

## RESEARCH ARTICLE

10.1002/2015JC010988

## Special Section:

Physical Processes  
Responsible for Material  
Transport in the Gulf of  
Mexico for Oil Spill  
Applications

## Key Points:

- Frontal processes dominate in overall plume mixing
- Frontal zone produces elevated near-surface turbulent kinetic energy dissipation rates
- Head wave detachment increases frontal mixing

## Correspondence to:

K. D. Huguenard,  
kimberly.huguenard@maine.edu

## Citation:

Huguenard, K. D., et al. (2016), On the nature of the frontal zone of the Choctawhatchee Bay plume in the Gulf of Mexico, *J. Geophys. Res. Oceans*, 121, 1322–1345, doi:10.1002/2015JC010988.

Received 19 MAY 2015

Accepted 18 JAN 2016

Accepted article online 25 JAN 2016

Published online 15 FEB 2016

© 2016. American Geophysical Union.  
All Rights Reserved.

## On the nature of the frontal zone of the Choctawhatchee Bay plume in the Gulf of Mexico

K. D. Huguenard<sup>1</sup>, D. J. Bogucki<sup>2</sup>, D. G. Ortiz-Suslow<sup>3</sup>, N. J. M. Laxague<sup>3</sup>, J. H. MacMahan<sup>4</sup>,  
T. M. Özgökmen<sup>3</sup>, B. K. Haus<sup>3</sup>, A. J. H. M. Reniers<sup>5</sup>, J. Hargrove<sup>3</sup>, A.V. Soloviev<sup>6</sup>, and H. Graber<sup>3</sup>

<sup>1</sup>Department of Civil and Environmental Engineering, University of Maine, Orono, Maine, USA, <sup>2</sup>Department of Physical and Environment Sciences, Texas A&M-Corpus Christi, Corpus Christi, Texas, USA, <sup>3</sup>Department of Ocean Sciences, University of Miami, Miami, Florida, USA, <sup>4</sup>Oceanography Department, Naval Post Graduate School, Monterey, California, USA, <sup>5</sup>Department of Hydraulic Engineering, Delft University of Technology, Delft, Netherlands, <sup>6</sup>Department of Marine and Environmental Sciences, Nova Southeastern University, Fort Lauderdale, Florida, USA

**Abstract** River plumes often feature turbulent processes in the frontal zone and interfacial region at base of the plume, which ultimately impact spreading and mixing rates with the ambient coastal ocean. The degree to which these processes govern overall plume mixing is yet to be quantified with microstructure observations. A field campaign was conducted in a river plume in the northeast Gulf of Mexico in December 2013, in order to assess mixing processes that could potentially impact transport and dispersion of surface material near coastal regions. Current velocity, density, and Turbulent Kinetic Energy Values,  $\varepsilon$ , were obtained using an Acoustic Doppler Current Profiler (ADCP), a Conductivity Temperature Depth (CTD) profiler, a Vertical Microstructure Profiler (VMP), and two Acoustic Doppler Velocimeters (ADVs). The frontal region contained  $\varepsilon$  values on the order of  $10^{-5} \text{ m}^2 \text{ s}^{-3}$ , which were markedly larger than in the ambient water beneath ( $0 \text{ } 10^{-9} \text{ m}^2 \text{ s}^{-3}$ ). An energetic wake of moderate  $\varepsilon$  values ( $0 \text{ } 10^{-6} \text{ m}^2 \text{ s}^{-3}$ ) was observed trailing the frontal edge. The interfacial region of an interior section of the plume featured opposing horizontal velocities and a  $\varepsilon$  value on the order of  $10^{-6} \text{ m}^2 \text{ s}^{-3}$ . A simplified mixing budget was used under significant assumptions to compare contributions from wind, tides, and frontal regions of the plume. The results from this order of magnitude analysis indicated that frontal processes (59%) dominated in overall mixing. This emphasizes the importance of adequate parameterization of river plume frontal processes in coastal predictive models.

### 1. Introduction

In May 2010, the Deepwater Horizon Oil Spill released 4.4 million barrels of unprocessed crude oil into the Gulf of Mexico [Crone and Tolstoy, 2010]. This environmental disaster motivated research into accurately predicting the fate and transport of oil in the ocean. Given the distance between oil platforms and the coast, accurate prediction requires the understanding of the complex interaction between near-surface processes in an open ocean, inner shelf, and surf zone. The highest social-economic impact of the oil spill occurred at the coast [Smith et al., 2010; Morris et al., 2013], which underscores the importance of correctly representing coastal processes in predictions. In order to adequately predict oil fate, the behavior of turbulence must be understood at all wavenumbers, ranging from large horizontal length scales typically associated with geophysical processes to the Kolmogorov dissipative scales. Turbulence plays an important role in many near-surface processes, such as controlling gas transfer across the air-sea interface [Chickadel et al., 2011], enhancing biological productivity [Gruber et al., 2011], and vertically mixing oil in breaking waves [Tkalic and Chan, 2002]. In the field, small-scale turbulence can be readily evaluated by measuring Turbulent Kinetic Energy (TKE) dissipation rates,  $\varepsilon$ .

The coastal region of the Gulf of Mexico (Figure 1a) has a complex system of estuarine outlets, where the associated processes span far beyond inlet regions. Figure 1b shows a NASA MODIS ocean color satellite image that showcases how riverine material can be transported across the inner shelf in a strongly eddying regime. Colder, fresher water from estuarine outlets (e.g., discharge from the Mississippi delta) tend to fill the coastal regions of the Gulf of Mexico and could potentially act as a barrier for oil transport from the ocean to the coast [Kourafalou and Androulidakis, 2013].

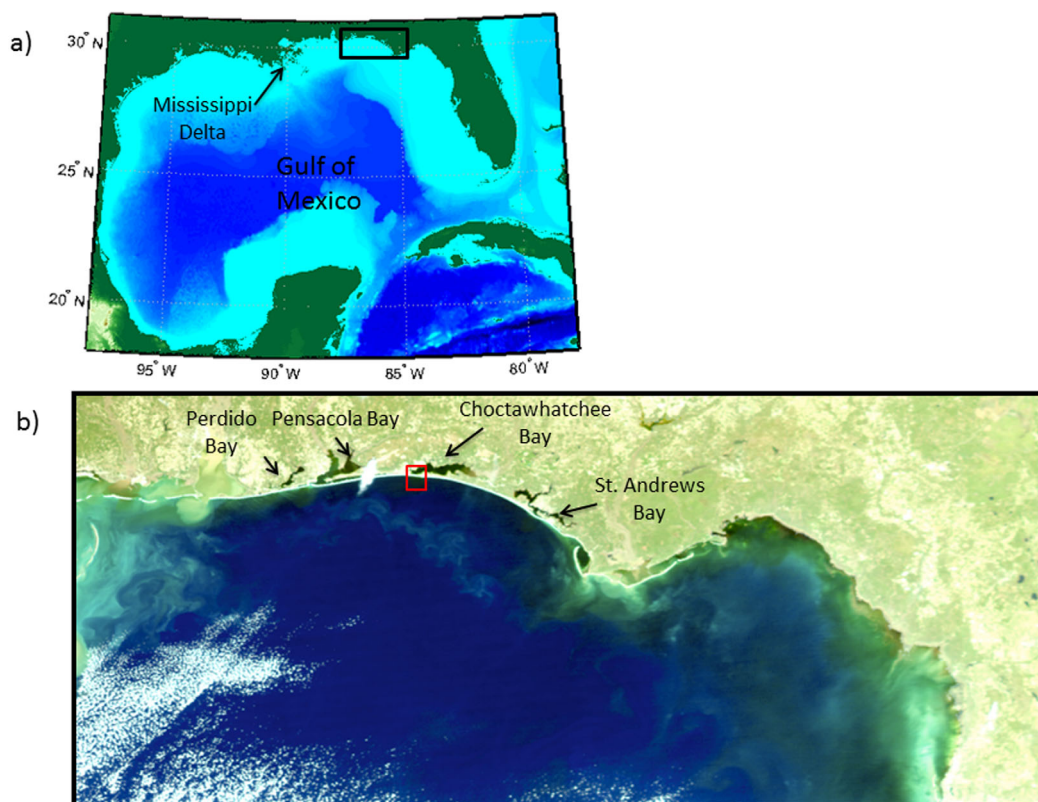


**Figure 1.** (a) Map of the Gulf of Mexico. Black box denotes location of (b) ocean color from MODIS-AQUA obtained on 16 December 2013. Red box outlines study area location.

Field observations of river plumes are not well documented in this region, but are clearly important for surface material transport. River plumes are an expanding volume of freshwater that radially spreads into coastal waters. They are sometimes referred to as fronts or buoyant gravity currents because they are driven by density gradients, but can be influenced by external factors like river discharge, tides, ambient currents, wind, and Coriolis [Horner-Devine *et al.*, 2009].

The front of the river plume often features strong flow convergence and downwelling [O'Donnell *et al.*, 1998], which feeds a turbulent, rotor-like circulation immediately following the bounding edge of the plume [Luketina and Imberger, 1989]. Essentially representing the “head wave” (or internal bore) of a buoyant gravity current [Marmorino and Trump, 2000; Stashchuk and Vlasenko, 2009; Jay *et al.*, 2009], the bore head is a propagating internal hydraulic jump that is characterized by a step-like variation in the height of a two-layer interface followed by intense short-period oscillations [Wang and Gao, 2000]. This frontal region is important because it can influence the dynamics of the interior of the river plume [O'Donnell *et al.*, 1998], as it generates high  $\varepsilon$  rates ( $10^{-4} \text{ m}^2 \text{ s}^{-3}$  in Orton and Jay [2005],  $10^{-3} \text{ m}^2 \text{ s}^{-3}$  in Kilcher and Nash [2010]) and strong mixing [Luketina and Imberger, 1989]. The dilution of plume water in the adjacent coastal region can occur through a variety of mixing processes, such as mixing in the frontal region, wind, tidal flow interacting with the bottom, and interfacial friction at the base of the plume. Pritchard and Huntley [2006] found that in the small-scale (in terms of river discharge) River Teign plume, the frontal region was capable of mixing the entire buoyancy input and was much larger than contributions from wind and tides. In their mixing and energy budget, the frontal mixing was indirectly evaluated using Garvine's equation [Garvine, 1984, equation (A3)]. Additionally, an order of magnitude analysis considered interfacial mixing negligible. These results could be verified using TKE dissipation rates to quantify mixing in the frontal region to confirm this assertion.

The frontal zones of river plumes have also been linked to coastal internal waves, which propagate beneath the surface of the ocean along density interfaces [Nash and Moum, 2005; Kilcher and Nash, 2010]. Ambient water stratification is required for river plumes to create internal waves [Stashchuk and Vlasenko, 2009].

However, residual plume waters can remain in the adjacent coastal region over multiple tidal cycles [Horner-Devine *et al.*, 2009], which makes internal waves prevalent in these regions [Jay *et al.*, 2009]. Stashchuk and Vlasenko [2009] used a numerical model to investigate generation mechanisms of internal waves from river plumes. They observed the formation of a solibore, which featured a step-like variation in salinity (the gravity current head) followed by a newborn packet of internal waves. When the internal wave amplitude is large enough, they can radiate away from bore head through a wave fission process described by Nash and Moum [2005]. Stashchuk and Vlasenko [2009] also found that the bore head might detach from the river plume and eventually transform into a small amplitude internal wave without nonlinear steepening and disintegration into a solitary wave packet.

The convergence zones of river plumes are characteristically narrow, less than 5 m wide [O'Donnell *et al.*, 1998], with bore heads featuring cross-sectional length scales around 150 m [Luketina and Imberger, 1987]. Due to grid resolution, river plume-related processes such as internal waves and bore heads feature narrow lengths that are not captured in coupled atmosphere-wave-ocean models. During the Surfzone Coastal Oil Pathways Experiment (SCOPE- <http://carthe.org/scope/>), ocean model grids varied from 0.05 to 4 km, while coastal model grids were somewhat finer with roughly 20 m cell sizes. To adequately resolve propagation and turbulence in a coastal model, grid sizes need to be  $\ll 1$  m. Inclusion of these fine-scale processes is typically done via subgrid-scale parameterizations [St. Laurent *et al.*, 2012].

Frontal regions of river plumes have been shown to dominate in terms of overall plume water mixing, where the frontal region was evaluated indirectly [Pritchard and Huntley, 2006]. Would in situ measurements of turbulence also yield frontal mixing values that dominate over other mechanisms? In this work, we build upon this understanding by quantifying frontal zone mixing using near-surface microstructure observations rather than a simplified parameterization based on the velocity relationship between the ambient water and river plume. To evaluate river plume mixing from frontal processes, wind and tides, measurements including current velocities, TKE dissipation rates, density, and wind speed were collected near a river plume coastal northwest Florida in December 2013. Typical rates of  $\varepsilon$  are quantified from two distinct instruments near the surface in the frontal region. These values are used to quantify mixing contributions from the aforementioned mechanisms to assess their influence on overall plume mixing.

## 2. Experimental Background

### 2.1. Study Site

The study site was located  $\sim 7$ – $8$  km west of Destin Inlet. This inlet is part of the Choctawhatchee River-Estuary system, which is the main source of freshwater discharge in addition to several creeks, springs, and ground water upwelling from the Floridian Aquifer [Ruth and Hadley, 2006]. Choctawhatchee Bay is a shallow, stratified system containing low tidal energy and limited flushing [Baylock, 1983; Livingston, 1986]. The mean annual discharge in 2013 (USGS station 02366500) was  $260 \text{ m}^3 \text{ s}^{-1}$ . Choctawhatchee Bay is 43 km long and follows an east-west orientation connecting the Gulf Intracoastal Waterway in the east to Santa Rosa Sound in the west. Tidal forcing is diurnal [Seim *et al.*, 1987] with small tidal ranges from 0.15 to 0.5 m between neap and spring tides, respectively.

### 2.2. Data Collection

Choctawhatchee River discharge measurements were obtained from United States Geological Survey station (#02366500) in Bruce, FL (Figure 2a). Tides were evaluated using water elevation data (from mean sea level) obtained from nearby Panama City National Oceanic and Atmospheric Administration (NOAA) station (#8723108). Fifteen minute wind data were acquired from a portable meteorological tower located 10 m above the ground at Beasley Park (Figure 2a).

The University of Miami's research vessel, named the Surface Physics Experimental Catamaran (SPEC), was used to obtain current velocities, hydrographic data, and  $\varepsilon$ . The SPEC bow was outfitted with a custom built framework, which enabled the secure mounting of various oceanographic and atmospheric sensors (Figure 3a). Real-time data acquisition occurred in the SPEC cabin, where a GPS-linked time synchronization server was used to guarantee simultaneously sampling of the various acquisition systems. For further details on the data collection and orientation of instruments on the SPEC, see Ortiz-Suslow *et al.* [2015a,b].

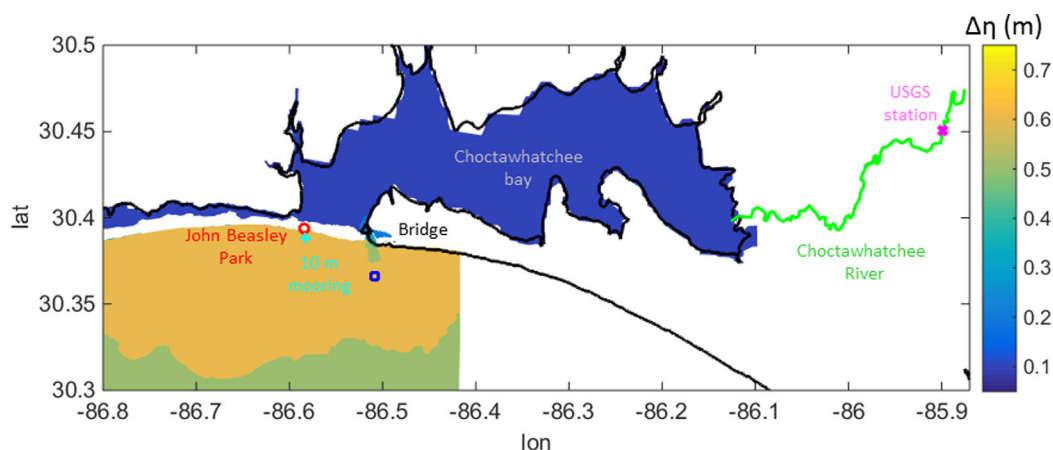


**Figure 2.** Study area map depicting the Delft 3-D model domain. Contours display 17 December tidal range. Magenta cross denotes river discharge measurement location, red circle indicates John Beasley Park where wind tower was positioned, cyan plus represents the location of the 10 m mooring. Black triangle is the water level measurement location at the bridge. Green line is the Choctawhatchee River and black outline is high-resolution shoreline data retrieved from *Wessel and Smith* [1996].

A 1200 kHz RDI Acoustic Doppler Current Profiler (ADCP) was mounted downward facing and collected profiles of current velocity at 0.8 Hz (Location A in Figure 3a). Data were collected in 0.25 m bins with a 0.5 m blanking distance between the instrument and the first bin at 0.61 m. The ADCP also included a temperature sensor, which provided near-surface ( $\sim 0.1$  m) observations (Location D in Figure 3a). An Ultrasonic Distance Meter (UDM) measured sea surface elevations at 50 Hz and was used to evaluate the surface wave environment. A YSI Castaway Conductivity Temperature Depth (CTD) profiler sampled conductivity and temperature at 5 Hz as it was lowered to the bottom. TKE dissipation rates were estimated using two instruments: a Rockland Scientific Vertical Microstructure Profiler (VMP) that sampled at 512 Hz and two Sontek Acoustic Doppler Velocimeters (ADV) that sampled at 20 Hz. The ADVs were mounted vertically at 0.14 and 0.41 m below mean water level and jutted ahead of the bow of the boat to ensure there was no flow interaction from the boat (Location B in Figure 3a). The VMP was deployed in a novel uprising manner to collect velocity shear data near the surface (The ADVs were mounted vertically at 0.14 m and 0.41 m below mean water level and jutted ahead of the bow of the boat to ensure there was no flow interaction from the boat (Figure 3b). The VMP was fitted with a floatation collar and lowered bottom first with a weighted cannon ball and release mechanism. After the release, mechanism reached the bottom and bubbles were no longer visible, the instrument ascended toward the surface at speeds near  $\sim 0.6 \text{ m s}^{-1}$ . It took roughly 1 m for the instrument to reach an approximate constant velocity, which limited the deepest meter of vertical resolution. Unfortunately, the temperature and conductivity sensors on the VMP were flooded and collocated  $\varepsilon$  and  $\rho$  values could not be achieved. To compare consistency of the ADV and VMP measurements, two profiles are presented in Figure 3c, which represent the construction of  $\varepsilon$  profiles from both instruments. One profile was collected inside of the bore (green in Figure 3c) and a second was collected in the trailing wake (red in Figure 3c). The comparison showed that  $\varepsilon$  decayed logarithmically with depth, which was consistent with a shear wall surface layer scaling [*Csanady*, 1984] and was supported by velocity observations. This indicated that the two distinct  $\varepsilon$  measurements were less than half an order of magnitude of one another.

On 17 December, the bore head of the Choctawhatchee Bay plume was visually identified as a band of surface roughness oriented with the shore-normal and propagating westward away from Destin Inlet (Figure 4). In order to sample this frontal region, the vessel was positioned ahead (west) of the surface signature and cross-sectional observations were made as the disturbance propagated westward underneath the SPEC. A total of three transects that capture the frontal zone were completed (green, pink, and red lines in Figure 4). CTD and VMP casts were collected while the ADCP and ADVs sampled continuously from the SPEC bow-framework. A final transect (blue in Figure 4) was conducted toward the inlet that measured the alongshore extent of the river plume. One final VMP cast was conducted halfway through this river plume transect.

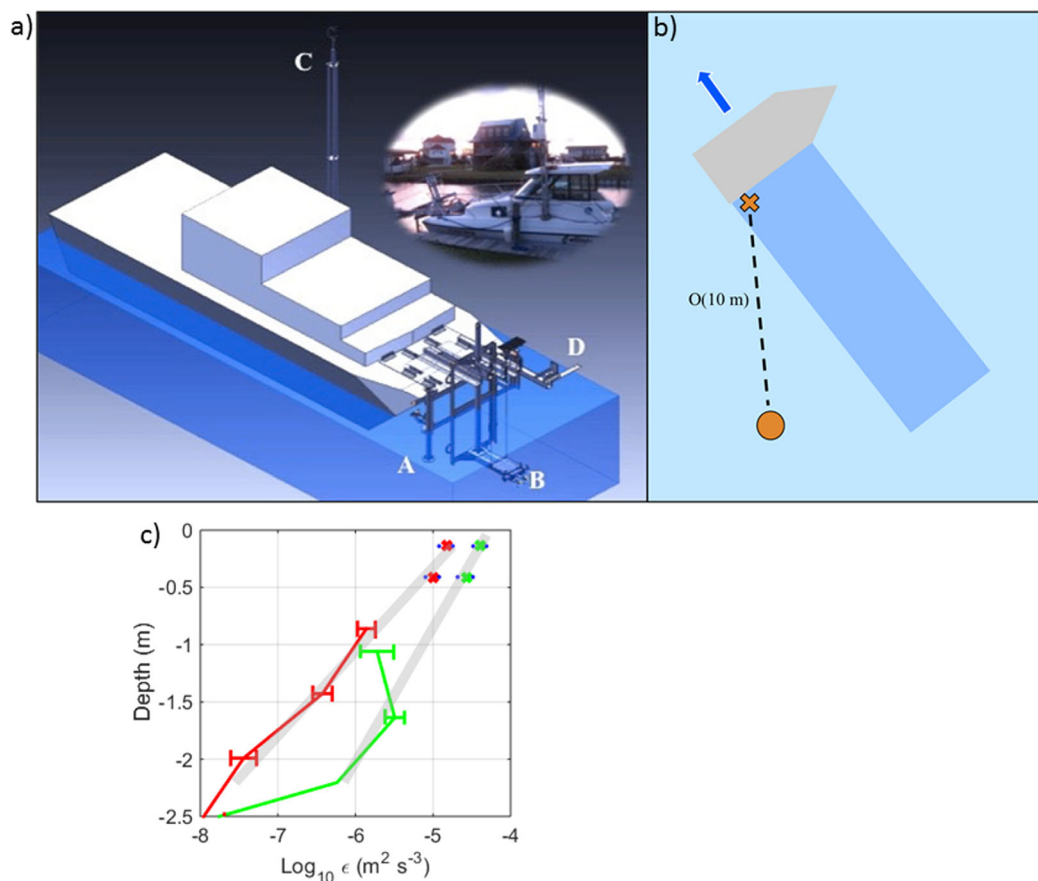


**Figure 3.** (a) Adapted from *Ortiz-Suslow et al.* [2015b], this shows a technical schematic of the research vessel, SPEC, used for the observations and the deployment and recovery of the VMP. Within this schematic several instruments are highlighted: the (A) mounting location of the ADCP, (B) the location of the ADV's—note these moved for this experiment to the just below the surface on the portside, (C) the sonic anemometer mast, and (D) the mounting plate for the UDM. (b) A cartoon depicting a typical VMP deployment (cross) recovery (circle). The blue arrow denotes the estimated “forcing” direction on SPEC, i.e., the predicted drift of the vessel. This was ascertained via observation and real-time data output from the ADCP. For scale, the SPEC freeboard is 1 m. (c) TKE dissipation profile comparing VMP (line) and ADV (x symbol) measurements from Transect 1 inside the bore (green) and Transect 2 in the bore wake (red). The grey line indicates the linear extrapolation of ADV values to comparable VMP depths and blue dots indicate uncertainty bounds for ADV measurements.

## 2.3. Data Processing

### 2.3.1. TKE Dissipation Rate, $\varepsilon$

Acoustic and microstructure methods were used to evaluate  $\varepsilon$ . The rate of Turbulent Kinetic Energy (TKE) dissipation,  $\varepsilon$ , is proportional to the variance of velocity shear under the assumption that turbulence is homogenous and isotropic (equation (1)). The FFT-length (0.9 s) was chosen to resolve the lowest wave number of interest, in this case 0.5 m. Power spectra were calculated, from which any noise contamination from accelerations were removed using a Goodman coherent noise removal algorithm [Goodman *et al.*, 2006]. Assuming isotropic and homogeneous turbulence, values of  $\varepsilon$  were calculated by integrating the velocity shear spectrum,  $\psi$ , in wave number space following the well-accepted method of *Lueck et al.*, [2002]:

$$\varepsilon = \frac{15}{2} \nu \overline{\left(\frac{\partial u'}{\partial z}\right)^2} = \frac{15}{2} \nu \int \Psi(k) dk \quad (1)$$

where  $u'$  is the turbulent fluctuating velocity,  $\nu$  is the kinematic viscosity, and  $k$  is the wavenumber. Particular regions that exhibited large ( $> 5^\circ$ ) inclination angles from the vertical were not included. Profiles of  $\varepsilon$  from two shear probes were averaged together to represent a single vertical profile, and the uncertainties between these two profiles are presented as error bars around the mean profile.

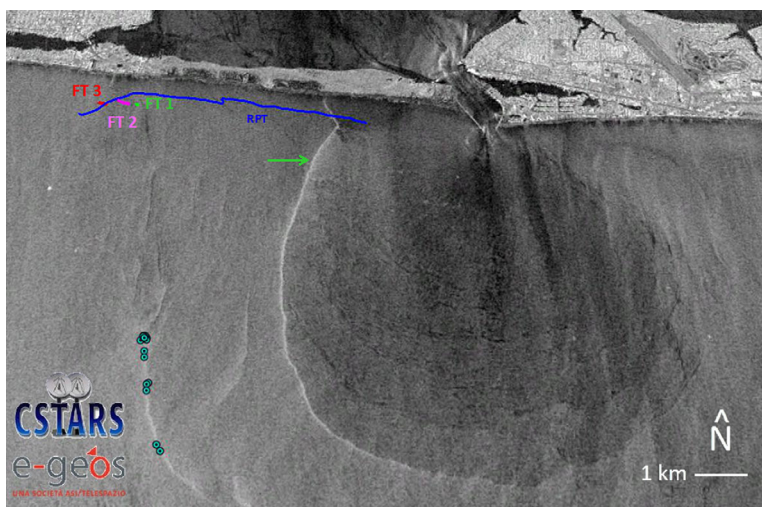


**Figure 4.** SAR image collected at 11:28:12 UTC on 17 December. Transect lines were collected after 6 h after SAR image. Blue line is the River Plume Transect (RPT). Green, magenta and red lines mark Frontal Transects (FT 1–3), respectively. Green arrow denotes 17 December tidal plume. Blue circles are drifters positioned in the convergence zone of a remnant plume front. COSMO-SkyMed™ Product ©ASI 2013 processed under license from ASI—Agenzia Spaziale Italiana. All rights reserved. Distributed by e-GEOS. Downlinked and processed by CSTARS.

The ADV data were despiked following the phase-space thresholding technique of *Goring and Nikora* [2002], where points outside of a three-dimensional ellipsoid were removed. The removed values were linearly interpolated following *Elgar et al.* [2005]. Values of  $\varepsilon$  were calculated from the vertical velocity spectrum (equation (2)), which was utilized for the reduced effect of instrument noise [*Feddersen et al.*, 2007] and minimized contamination by wave orbital velocities [*Huntley*, 1988; *Parra et al.*, 2014].

$$\varepsilon = 1.04 \left\langle \left( S_{w'w'}(k) k^{5/3} \right)^{3/2} \right\rangle \quad (2)$$

In equation (2),  $S_{w'w'}$  is the spectrum of vertical velocity fluctuations,  $k$  is the wavenumber, and  $\langle \rangle$  is the average in the inertial subrange. Frequency was converted to wavenumber following *Lien and D'Asaro* [2006], where the instantaneous velocity was used instead of the mean velocity to transform time into space. The method is equivalent to Taylor's frozen field hypothesis [*Lumley and Terray*, 1983], however does not require the mean flow to be 10 times greater than the perturbation velocity. Blocks of 5 min data were sectioned into 25 s, where data were detrended and Hanning windowed with 50% overlap, yielding power spectra that contained 124 degrees of freedom. Each individual spectrum was examined to locate the inertial subrange, which was well resolved. A measure was implemented to ensure  $\varepsilon$  estimates were not contaminated by flow interference from wake shedding off the boat. If the boat heading was outside of  $\pm 45^\circ$  into direction of the surface flow, the ADV measurements were discarded. A sensitivity analysis was conducted to determine the optimal block sizes used to calculate  $\varepsilon$ . Three time blocks were evaluated (3, 5, and 8 min), each consisting 12, 19, and 30 s window lengths, respectively. By using the block size of 2 min, the averaged spectrum of the segments was limited by small window sizes, where energy from larger eddies was not resolved. The 5 min block was selected because there was insignificant change in  $\varepsilon$  estimates between 5 and 8 min blocks of data. The ADV measurements were extrapolated to the shallowest VMP depths to compare the reliability of the two techniques. Figure 3cd displays an example comparison for two profiles: inside in the bore (Transect 1) and in the bore wake (Transect 2). The results compared favorably, where values were within less than half an order of magnitude of the linearly extrapolated projection.

### 2.3.2. Hydrographic Data

The ADCP data were averaged (15 ensembles per average) and data with  $< 85\%$  good and error velocities  $> 10 \text{ cm s}^{-1}$  were discarded. The deepest 10% of the profiles were removed to account for side lobe effects. The data were interpolated onto a uniform grid with 0.25 m bin and 13 s time resolutions and a 2-D nearest neighbor filter was used to smooth data. Echo intensity is often used to examine mechanisms such as flow convergence regions or internal waves [*Sandstrom et al.*, 1989; *Valle-Levinson et al.*, 2004; *Ross et al.*, 2014]

and the sound scattered in the ocean is often presented in terms of sound scattering strength,  $I(z, t)$  [Urlick, 1983].

$$I(z, t) = 10 \log_{10}(\text{Echo Intensity}) \quad (3)$$

The normalization of  $I(z, t)$  functions to account for bottom to surface attenuation and spreading losses [Rippeth and Simpson, 1998]:

$$ECHO_a = I(z, t) - \langle I(z) \rangle \quad (4)$$

$ECHO_a$  was calculated by subtracting the temporal mean (over observational period in this case) of the sound scattering strength from the instantaneous sound scattering strength. This particular echo intensity correction was used to simply identify regions of flow convergence.

The conductivity and temperature profiles were interpolated into 0.25 m bins, from which density was calculated. The Brunt-Vaisala (buoyancy) frequency, which was calculated using centered differences and is a proxy for stratification:

$$N = \sqrt{-\frac{g}{\rho_o} \frac{\partial \rho}{\partial z}} \quad (5)$$

where  $g$  is the gravitational acceleration ( $9.81 \text{ m s}^{-2}$ ) and  $\rho_o$  is the ambient density of seawater ( $1025 \text{ kg m}^{-3}$ ), and  $\rho$  is the instantaneous density.  $N$  represents the frequency at which a parcel of fluid oscillates in a medium and larger values signify increased stratification. The Richardson number was used to assess mixing conditions and represents the competition between stratification and vertical shear:

$$Ri = \frac{N^2}{S^2} \quad (6)$$

where  $S^2 = \left(\frac{\partial u}{\partial z}\right)^2 + \left(\frac{\partial v}{\partial z}\right)^2$  is the squared vertical shear,  $u$  and  $v$  are the east-west and north-south components of velocity, respectively, at corresponding CTD cast times. Typically in the ocean, a theoretical critical threshold of  $Ri = 0.25$  has traditionally separated conditions considered stable ( $Ri > 0.25$ ) from conditions with the potential to be mixed [Baumert et al., 2005]. However, recent studies support a higher critical threshold, ranging from  $0.25 < Ri < 1$  [Giddings et al., 2011]. Canuto et al. [2008] found that mixing in a stably stratified flow could exist up to  $Ri \sim O(100)$  and supports the idea of a no critical  $Ri$  threshold.

The UDM surface elevation data were despiked using the same method as the ADVs velocities. Values from 16.14 UTC to 17.5 UTC on 17 December were detrended and Hanning windowed with 50% overlap, providing 124 degrees of freedom. The significant wave height,  $H_{sig}$ , represents the average of the highest 1/3 of the wave height observations and was calculated using  $H_{sig} = 4 \text{std}(\eta)$ , where  $\text{std}$  is the standard deviation and  $\eta$  is the wave height. This straight forward approximation was used to obtain a general view of the wave environment.

### 2.3.3. Satellite Imagery

A Synthetic Aperture Radar (SAR) image was collected on 17 December at 11:26 UTC, utilizing VV polarization in Stripmap mode with a spatial resolution of 5 m (Figure 5). River plumes featuring convergence zones appear in SAR imagery as narrow, bright features due to high backscatter [Lyzena et al, 2004]. The convergence zone can be used to identify the plume footprint, which on 17 December, resembled a semi-ellipse shape on the western side and was characterized by an aspect alongshore extent ( $\sim 3.5 \text{ km}$ ) to the across-shore extent ( $\sim 7 \text{ km}$ ). The eastern half of the plume was obscured because of the lack of surface roughness from the convergence zone, because the river plume velocity acted in concert with the ambient flow. These observations, along with later in situ measurements were used to estimate the plume surface area corresponding to the measurements.

### 2.3.4. Numerical Model Simulation

A Delft 3-D numerical simulation was conducted for 17 December 2013 to determine the Choctawhatchee tidal range, used to quantify the Choctawhatchee Bay tidal prism. The bathymetry used in the model was from the NOAA Coastal Relief Model, which was combined with a small boat survey at Destin Inlet. The model was run for 17 days, from 1 to 17 December, where the spin up time was 2 weeks. The model was forced with moored pressure sensor observations at 10 m depth off the coast of Beasley Park (located at the cyan symbol in Figure 2) and river discharge values (magenta symbol in Figure 2) from the previously

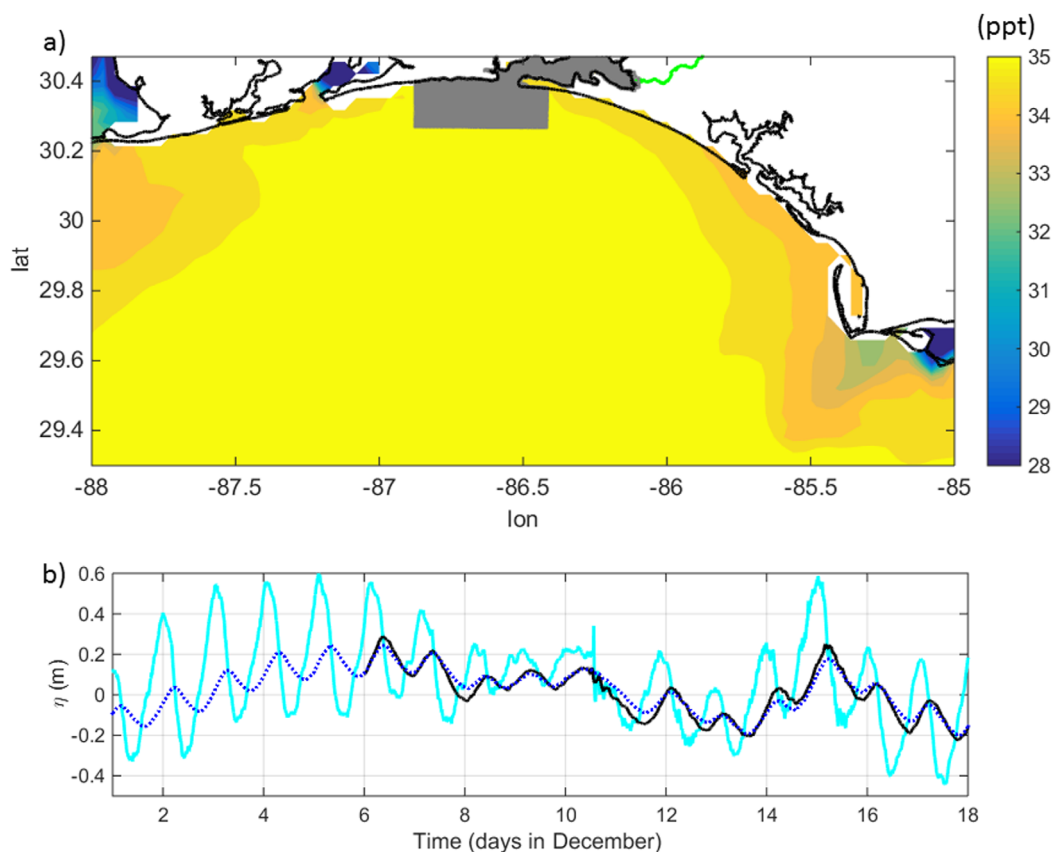


**Figure 5.** (a) HYCOM domain showing salinity in ppts. Grey shading represents the Delft 3-D domain. Green line is the Choctawhatchee River, (b) water level elevations from 10 m mooring (cyan), observations at the bridge (black), model predictions at the bridge (blue).

mentioned USGS station. The model simulation was conducted in baroclinic mode, with the initial salinity distribution ranging from 35 ppt outside of the bay and 21 ppt inside of the bay, which was considered to be fresh water. The ocean boundary salinity was set at 35 ppt using *Thatcher and Harleman* [1981] boundary conditions with a time lag of 6 h to account for the tidal pulsing of the plume.

The Delft 3-D model domain is shown in Figure 2, while the HYCOM domain is pictured in Figure 5a. The offshore boundary condition is a weakly reflective water level boundary, while the lateral boundaries are Neumann boundaries, where the slope in the surface elevation was obtained from the HYCOM simulation to represent the larger scale flow. The land side boundary condition is freshwater discharge at the far eastern end to represent river inflow. The grid resolution was variable, ranging from approximately 250 m offshore to 25 m in front of Beasley Park. A Manning friction formulation was used, with a Manning number of  $n = 0.028$ . The vertical resolution consisted of ten sigma layers in the vertical, representing 2,3,4,6,8,10,12,15,20% of the water depth from top-to-bottom. The higher resolution at the surface was implemented accommodate the presence of a thin surface layer. Wind waves were not included in the model runs and the model is hydrostatic.

Initial model verification was based on comparisons between a pressure sensor located at the bridge between Choctawhatchee Bay and the 24 h velocity transect observations collected on 9 December 2013 in *Valle-Levinson et al.* [2015]. The water elevation results from the model (blue in Figure 5b) were compared with the 10 m water elevations at John Beasley Park and at the bridge inside Destin Harbor (black in Figure 2). Figure 5b shows the measured elevation at the 10 m array location (cyan) corresponding to the offshore boundary condition and water elevations (black) at the bridge crossing the bay. This depicted a significant reduction in tidal amplitude and accompanying phase shift, as expected. Model prediction of the water level near the bridge is in green and indicated a good match with 95% confidence interval of  $\pm 3$  cm.

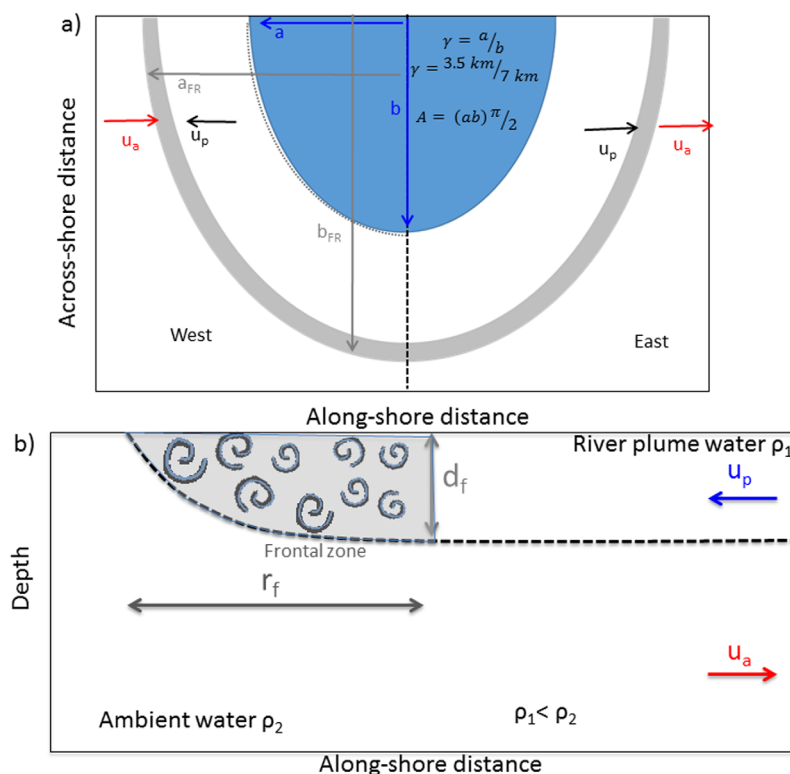


**Figure 6.** (a) Conceptual diagram depicted semi-elliptical assumed shape of plume. Grey denotes area used for frontal mixing estimate,  $u_p$  indicates the velocity of the plume,  $u_a$  indicates velocity of ambient water,  $a$  and  $b$  is the along (3 km) and across-shore (6 km) distance from the plume front to the inlet,  $a_{FR}$  and  $b_{FR}$  is the along and across-shore distances from the frontal zone to the inlet. Blue semi-ellipse reflects the area of the plume,  $A$ , corresponding to the SAR image in Figure 4, which was used to determine the aspect ratio,  $\gamma$ . (b) cross section of plume front where  $r_f$  is the length of the frontal zone and  $d_f$  is the depth of the frontal zone.

### 2.3.5. Simplified Mixing Budget

To evaluate overall plume mixing, a simplified budget was used to compare the relative importance of mixing power from tidal, wind, and frontal mixing [Pritchard and Huntley, 2006]. The power ( $W = \text{kg m}^2 \text{s}^{-3}$ ) due to barotropic tidal flow interacting with the bottom,  $P_t$ , was estimated from:

$$P_t = \delta \rho_2 C_D U_t^3 A \quad (7)$$

where  $\delta$  is the efficiency factor for tidal stirring (0.075),  $\rho_2$  is the ambient water density,  $C_D$  is the bottom drag coefficient (0.0025),  $A$  is the surface area of the plume (Figure 6a), and  $U_t$  is the barotropic tidal current, which was estimated from a temporal and depth average of the ambient waters ahead of the frontal zone. The value of  $\delta$  selected corresponds to the value observed in the Connecticut River plume [Valle-Levinson, 2010]. The plume area was approximated assuming that the plume symmetrically spread to the east and west out of the inlet. An aspect ratio ( $a/b \sim 0.5$ ) was calculated for the western half of semi-ellipse (grey dash line in Figure 6a), where the alongshore distance from the convergence zone to the inlet was approximately 3 km and the offshore distance was 6 km (Figure 6a) observed in the SAR image. It was assumed the plume spread symmetrically on east and west sides of the inlet, which was not verifiable by the SAR image. SAR images only detect regions of convergence, which likely did not occur in the east side of the plume given the eastward ambient current (red arrow in Figure 6a) acting in concert with the eastward plume velocity (black arrow in Figure 6a). This assumption is supported by the modeling results of Xia *et al.* [2011] at nearby Perdido Bay, which depicted plume that spread similarly on east and west sides, with only a slight westward biased under no wind forcing. Our measurements concluded  $\sim 8$  km ( $a_{FR}$  in Figure 6b) west of Destin Inlet and using the 0.5 aspect ratio, we estimated that the across-shore length was  $b_{FR} = 16$  km (grey arrow in Figure 6a).

The power of the wind stress was determined:

$$P_w = \zeta \rho_a W_{10} U_{10}^3 A \quad (8)$$

where  $\zeta$  is an efficiency factor for wind stirring (0.023),  $\rho_a$  is the density of air,  $W_{10}$  is a wind drag coefficient (0.00145), and  $U_{10}$  is the wind speed, which was the temporal mean speed during the observations.

The frontal zone mixing power,  $P_{FR}$ , was calculated from the volume integral of a narrow band around the perimeter of a semi-ellipse (grey band in Figure 6a):

$$P_{FR} = \rho_2 A_{FR} \int_0^{d_f} \varepsilon dz \quad (9)$$

where  $A_{FR} = \left(\frac{\pi}{2} a_{FR} b_{FR}\right) - \left[\frac{\pi}{2} (a_{FR} - r_f)(b_{FR} - r_f)\right]$  (grey band in Figure 6b)  $a_{FR}$  is the alongshore distance from the frontal zone to the inlet,  $b_{FR}$  is the across-shore distance from the frontal zone to the inlet,  $r_f$  is the width of the frontal zone (Figure 6b), and  $d_f$  the depth of the frontal zone (Figure 6b).

The power required to instantaneously mix the plume can be determined from:

$$P_B = \frac{(h - d_{in})}{2} \Delta \rho g Q_b \quad (11)$$

where  $h$  is the water depth near the inlet,  $d_{in}$  is the plume depth near the inlet,  $\Delta \rho$  is the difference between the plume density near the inlet and ambient water density, and  $Q_b$  is the instantaneous brackish discharge rate at the inlet. The details of how these parameters were estimated from the measurements are outlined in the results section and uncertainties are detailed in the discussion. An analysis was conducted on the sensitivity of the various parameters and is detailed in the Appendix A.

### 3. Results

In this section, the tidal, wind, and river discharge conditions are presented, which highlight a quiescent surface environment during in situ observations. A satellite image in Figure 2 shows the river plume footprint approximately 6 h before in situ measurements. Next, the frontal zone observations depict a gravity current head, which appears to be detached from the main body of the river plume. The river plume observations are displayed, which were collected following the frontal zone measurements. To explore if the stratification ahead of the front could support detachment, gravity current solutions are evaluated under varying potential ambient water conditions. Last, a mixing budget is performed to compare mixing power from the frontal zone, wind, and tides.

#### 3.1. Environmental Conditions

Throughout the in situ observations collected on 17 December (orange boxes in Figure 7), winds were very weak ( $< 2 \text{ m s}^{-1}$ ) and fluctuated on and offshore (Figure 7a). Figure 7b displays relatively moderate river discharge values ( $150 \text{ m}^3 \text{ s}^{-1}$ ) as compared to the monthly minimum ( $130 \text{ m}^3 \text{ s}^{-1}$ ). The field measurements occurred during the largest spring tide of the month, which forced a 0.65 m tidal range (blue in Figure 7c). The spring tide enhanced ebb tidal velocities and combined with moderate river discharge values, provided moderate outflow of the Choctawhatchee Bay plume on 17 December.

The Choctawhatchee Bay plume radially spread into the adjacent coastal ocean and was identifiable in the SAR image by convergence lines (white streaks) located offshore and to the west (green arrow in Figure 4). Drifters were released at two locations near John Beasley Park on 16 December between 9:22 UTC and 18:00 UTC (grey box in Figure 7c). Their positions during the 17 December SAR image, collected at 11:28 UTC, (cyan circles in Figure 4) showed that they congregated along the convergence zone of the 16 December remnant plume front.

The surface wave environment on 17 December was extremely calm, as shown in photo taken at 15.7 UTC (Figure 8a). Wind speeds at 10 m above John Beasley Park were less than  $2 \text{ m s}^{-1}$  (Figure 8b) during transect observations, which indicated that near-surface TKE dissipation rates that would arise from wind stress should be of the order  $10^{-9} \text{ m}^2 \text{ s}^{-3}$  using the law of the wall dissipation scaling [Csanady, 1984]. A significant wave height of 0.20 m with dominant wave periods between 2 and 3 s was observed (determined from frequency in Figure 8c). Cumulatively, these observations described a very weak surface wave

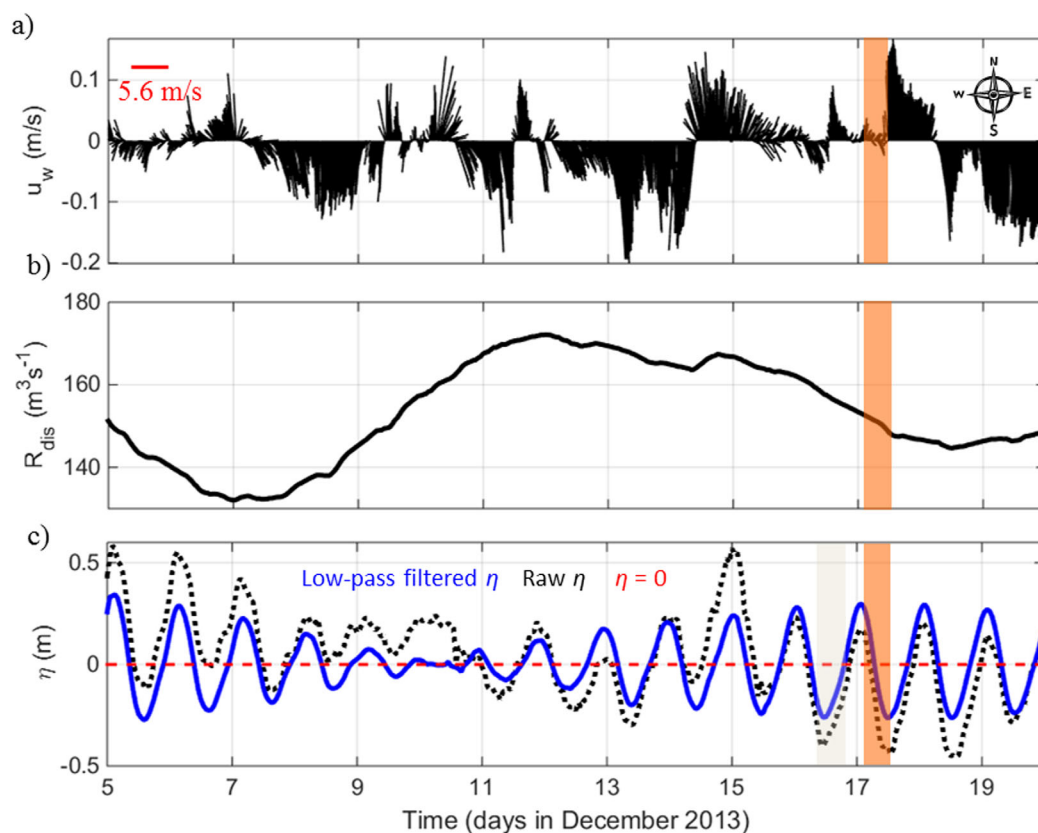


**Figure 7.** December environmental conditions time series: (a) scaled wind velocities, red line denotes 5.6 m/s, (b) Choctawhatchee River discharge values, and (c) water level elevation. Blue line is filtered at 30 h to remove low frequency variability, black is the original water level elevation signal. All times are in UTC. Orange boxes correspond to in situ observations on 17 December. Grey box indicates range when drifters in Figure 4 were deployed.

environment. The surface conditions during in situ observations were optimal for distinguishing  $\varepsilon$  inside the frontal region from the negligible stresses contributed from surface waves and winds.

### 3.2. Frontal Transect Observations

The frontal observations are separated into three classifications separated by spatial variability away from the inlet: Transect 1 (FT1 in Figure 4) was closest to the inlet, Transect 2 (FT2 in Figure 4) was near the Okaloosa Island Fishing Pier, and Transect 3 (FT3 in Figure 4) was west of the Pier. Transect 1 was collected earliest in time. Maps showing the spatial location of each transect are shown in Figure 9, which include ribbon plots displaying near-surface temperature, symbols that indicate CTD and VMP casts, times corresponding to when the VMP was deployed, and black arrows that conceptually denote the direction of boat movement. The orange arrows indicate the beginning of the transects. These can be compared to the time series figures in the subsequent sections to provide a spatial context. In each frontal transect, observations began in the ambient water ahead of the frontal zone. The boat drifted with the ambient current toward the east (warm colors in temperature ribbon plot in Figure 9) and then back to the west when the frontal zone (cool colors in Figure 9) propagated past the boat, which is why the following observations are presented as a function of time rather than distance.

#### 3.2.1. Transect 1: Closest to the Inlet

Transect 1 is the most eastward line (green) in Figure 4. An abrupt decrease in surface temperature ( $16.7^{\circ}\text{C}$ – $14.6^{\circ}\text{C}$  in Figure 10a) was observed at 16.3 UTC and marks the beginning of the frontal zone. This indicated the water inside frontal zone was colder and fresher than the ambient coastal waters ahead. The gravity current head was observed as a pulse of westward surface flow ( $-0.20\text{ m s}^{-1}$ ) that propagated into opposing  $0.10\text{ m s}^{-1}$  eastward ambient currents (Figure 10c). The velocities in the frontal zone were dominated in the east-west direction, as indicated by small ( $< 0.10\text{ m s}^{-1}$ ) north-south velocities (Figure 10d). The bore head also featured elevated echo intensity anomaly values ( $\text{ECHO}_a > 1\text{ dB}$  in Figure 10e), which commonly

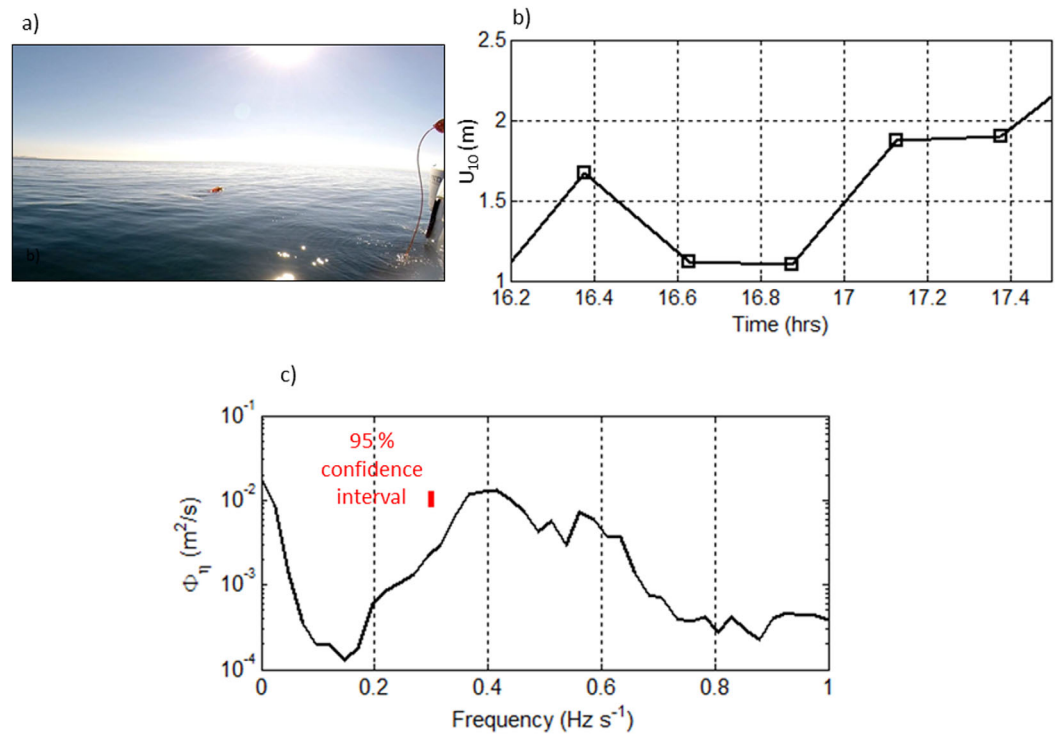


**Figure 8.** (a) Photo of VMP test profile collected at 15.7 UTC on 17 December showing calm surface conditions and a very weak wave environment, (b) wind speeds at  $U_{10}$  over John Beasley Park, (c) spectrum of sea surface elevation. Red line indicates 95% confidence interval.

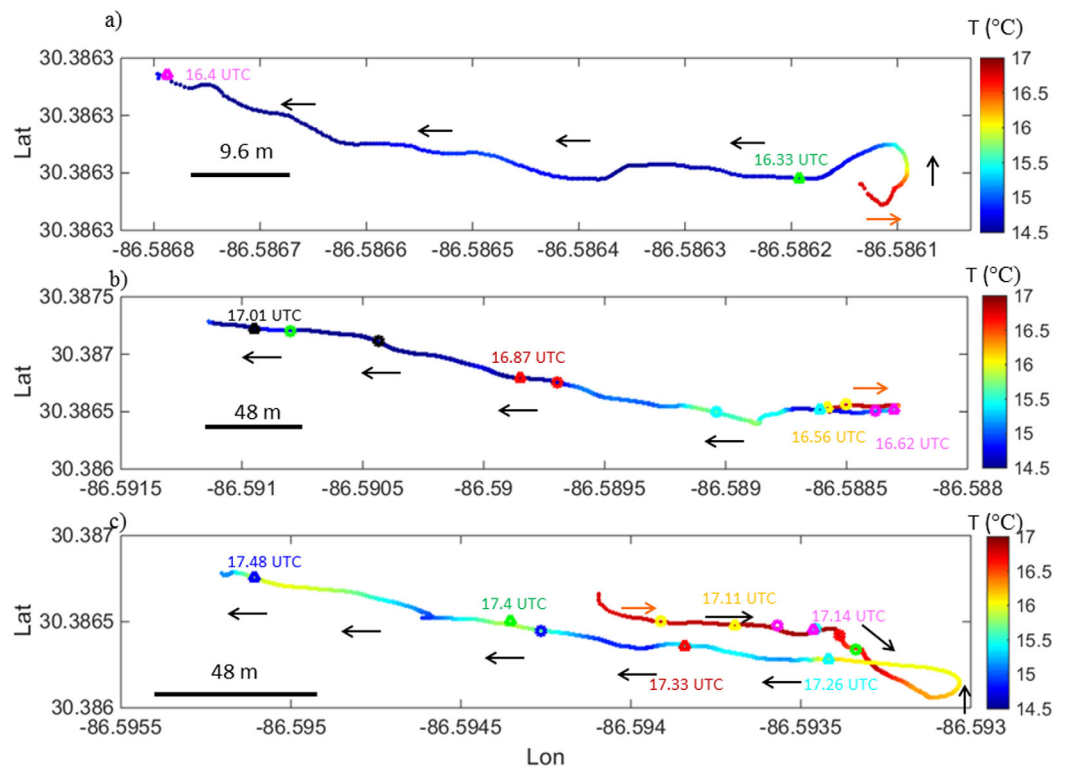


**Figure 9.** Map showing Frontal Transects (a) FT1, (b) FT2, (c) FT3. Colored ribbon denotes surface temperature, colored circles denote CTD casts, triangles are VMP casts. Black lines are spatial scales. Black arrows make the direction of boat drift and yellow arrow makes the initial direction. Times correspond with VMP casts.

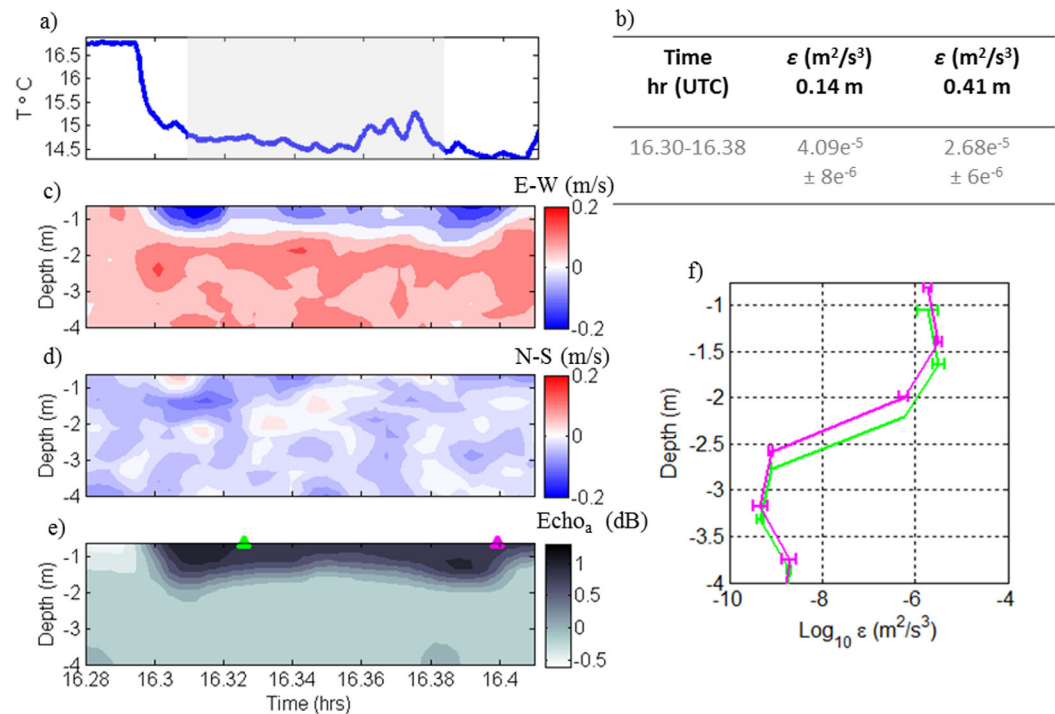


**Figure 10.** Frontal Transect FT1: (a) near-surface ( $\sim 0.10$  m) temperature. Grey box denotes timeframe used to calculate  $\varepsilon$  via ADVs; (b) table with  $\varepsilon$  via ADV at 0.14 and 0.41 m depths, values correspond to time frame denoted by grey box,  $\pm$  represents 95% confidence limits; (c) east (red) and west (blue) velocity contours; (d) north (red) and south (blue) velocity contours. The depth range has been truncated for plotting purposes and the actual depth is  $\sim 10$  m; (e) echo anomaly, triangles correspond to profiles in Figure 10f; and (f)  $\varepsilon$  profiles via VMP.

indicates the presence of flow convergence [O'Donnell *et al.*, 1998] and internal waves [Pan and Jay, 2009; Ross *et al.*, 2014]. The head appears to be detached at the eastward end ( $>16.4$  UTC) in terms of westward velocity, which was followed by near zero east-west velocities. This observation is further emphasized in the subsequent section 3.2.2.

The bore head produced very large near-surface  $\varepsilon$  values, ranging from  $4.06 \times 10^{-5} \text{ m}^2 \text{ s}^{-3}$  to  $2.64 \times 10^{-5} \text{ m}^2 \text{ s}^{-3}$  at 0.14 and 0.41 m depths (grey box in Figure 10a and table Figure 10b) even amidst weak wind and wave surface forcing. Two VMP casts complemented the ADV observations by providing the vertical structure of  $\varepsilon$  below 1 m (Figure 10f). The bore head was energetic and featured high  $\varepsilon$  values ( $3 \times 10^{-6} \text{ m}^2 \text{ s}^{-3}$ ) in the upper few meters, consistent with the vertical extent of the bore outlined by elevated ADCP echo intensity anomaly. Beneath,  $\varepsilon$  values were quite small ( $10^{-9} \text{ m}^2 \text{ s}^{-3}$ ), which were three orders of magnitude smaller than the 1 m depth values.

### 3.2.2. Transect 2: Near the Pier

Transect 2 (magenta in Figure 4) commenced in close proximity to the Pier and farther west than Transect 1. Across the bore head, Froude numbers were calculated (green in Figure 11a),  $Fr = u/c$ , where  $u$  is the depth-averaged velocity in the upper layer (1 m) and  $c$  is the first mode internal wave speed, determined from the Taylor-Goldstein Equation following Smyth *et al.* [2011]. All the values used in calculating  $Fr$  are outlined in Table 1. The flow regime transitioned from supercritical ( $>1$ ) ahead of the bore to subcritical ( $<1$ ) inside the bore because larger  $c$  values accompanied the freshwater introduced by the frontal zone. This  $Fr$  characterization differs from those typically used to determine conditions for internal wave radiation from river plumes, because the velocities reflect the average velocity of the upper layer instead of the translational speed of the river plume. This particular  $Fr$  characterization highlights a flow regime shift across the bore head. The bore wake featured supercritical values, which indicated dynamical differences between the bore ( $Fr < 1$ ) and bore wake ( $Fr > 1$ ). A relatively large  $Fr$  ( $>10$ ) value was calculated in the ambient water because the water column was very weakly stratified and contained very small  $c$  ( $<0.01 \text{ m s}^{-1}$ ).

As the bore head propagated westward, Transect 2 captured more of the energetic wake than in Transect 1. The wake featured very small east-west velocities that fluctuated around zero (Figure 11c), which

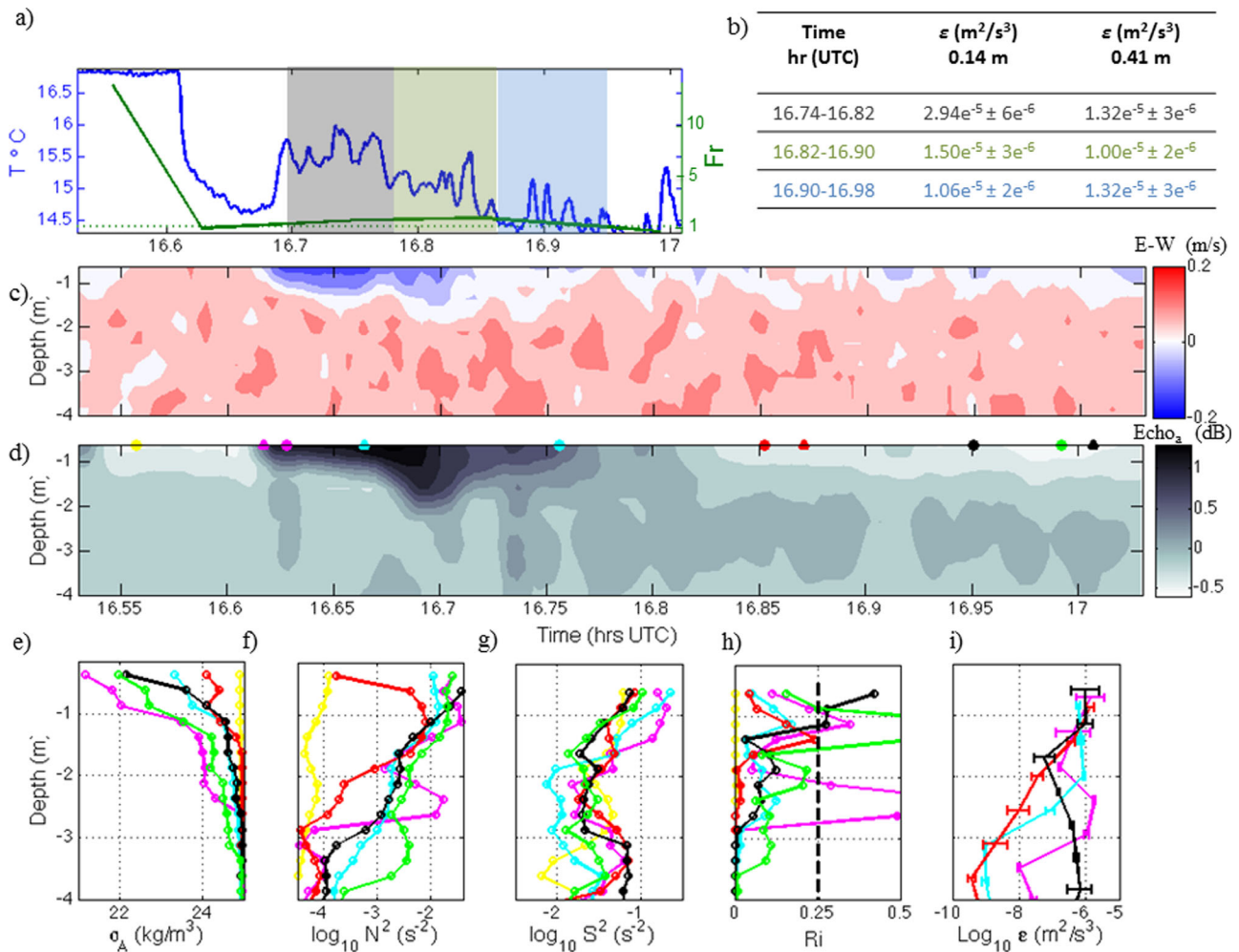


**Figure 11.** Frontal Transect FT2: (a) near-surface (~0.10 m) temperature (blue) and Froude number (green). Grey boxes mark periods corresponding to ADV  $\epsilon$  estimates; (b) table with  $\epsilon$  via ADV at 0.14 and 0.41 m depths, grey-colored values correspond to time frame denoted by grey, green, and blue boxes,  $\pm$  represents 95% confidence limits; (c) east (red) and west (blue) velocity contours. The depth range has been truncated for plotting purposes and the actual depth is ~10 m; (d) echo intensity anomaly, triangles denote VMP casts in Figure 11h and circles mark CTD casts in Figure 11e; (e) density anomaly,  $\rho - 1000$ ; (f) buoyancy frequency presented on a log base 10 scale; (g) squared vertical shear  $S^2$ ; (h) Richardson number, black line is  $Ri = 0.25$ , values  $>0.25$  stable conditions and  $<0.25$  denotes conditions for mixing; and (i) TKE dissipation rates.

indicated a discontinuity in westward velocity between the internal bore and the trailing river plume. This indicated the bore detached from the river plume in terms of westward velocity. The wake also featured rapidly fluctuating temperature values that supported an active surface region (Figure 11a). The ADVs depicted moderate  $\epsilon$  values (grey boxes Figure 11a and table in Figure 11b) in the wake, which ranged from  $1.0 \times 10^{-5} m^2 s^{-3}$  to  $2.9 \times 10^{-5} m^2 s^{-3}$  (0.14 m) and  $1.0 \times 10^{-5} m^2 s^{-3}$  to  $1.32 \times 10^{-5} m^2 s^{-3}$  (0.41 m) and were marginally smaller than the values collected inside the bore head during Transect 1.

**Table 1.** Froude Number Parameters for FT1 and FT2<sup>a</sup>

Time (UTC)	u (m/s)	c (m/s)	Fr
16.55	0.11	0.008	13.80
16.63	0.13	0.15	0.87
16.75	0.13	0.08	1.62
16.85	0.10	0.05	1.80
16.95	0.07	0.07	1
16.99	0.07	0.125	0.56
17.09	0.075	0.03	2.5
17.12	0.137	0.03	4.5
17.14	0.10	0.02	5
17.15	0.09	0.09	1
17.18	0.10	0.059	1.7
17.39	0.13	0.09	1.4

<sup>a</sup>u is the depth-averaged speed in the upper 1 m, c is the first mode internal wave speed, Fr is the Froude number.  $Fr > 1$  is supercritical,  $Fr < 1$  is subcritical.

The vertical shape of the internal bore changed, as revealed by the echo intensity anomaly observations (Figure 11d). The leading edge was shallower

than in the previous transect, while the deepest section was located toward the center of the bore (16.7 UTC). The ambient conditions ahead of the bore were very weakly stratified, indicated by a density profile with top to bottom density values ranging from 1024.9 to 1025 kg m<sup>-3</sup> (yellow profile in Figure 11e). Inside the bore, the water column was stratified and featured top-to-bottom density values ranging from 1021 to 1025 kg m<sup>-3</sup> (magenta in Figure 11e).

Trailing the edge of the bore (cyan in Figure 11e), the near-surface layer was less stratified and featured an upper layer value of 1023.2 kg m<sup>-3</sup>. Toward the end of the transect, the upper layer density was reduced (green and black in Figure 11d), likely representing the freshwater lens of the trailing plume. The temporal variation in near-surface density also evidenced bore detachment from the river plume and yielded a frontal zone length of ~260 m.

Conditions for mixing were confirmed by low Richardson number values ( $Ri < 0.25$ ), which were below the critical value ( $Ri = 0.25$ ) at most locations (Figure 11h). Stable conditions were identified at 1 and 2 m depths in three casts (magenta, green, and black), which marked the interface between fresh and ambient waters. Predominantly mixed conditions ( $Ri < 0.25$ ) were supported by nearly uniform density profiles below 2 m weak stratification  $N^2 (< 10^{-2} \text{ s}^{-2})$  in Figure 7f), and large  $S^2 (> 10^{-2} \text{ s}^{-2})$  in Figure 11g). Inside the bore head (magenta and cyan profiles in Figure 11i), large  $\varepsilon$  values ( $10^{-6} \text{ m}^2 \text{ s}^{-3}$ ) were confined to the upper 3 m. Active mixing was supported in the surface region of the final profile (red in Figure 11i), which was collected in the wake of the bore and displayed the largest  $\varepsilon$  values ( $1 \times 10^{-6} \text{ m}^2 \text{ s}^{-3}$ ) at the surface that linearly decreased with depth. Overall, Transect 2 indicated that the bore head was detached from the river plume and dispersive, leaving a turbulent region in the wake that supported a wider frontal mixing zone.

### 3.2.3. Transect 3: West of the Pier

The final frontal transect began in the very weakly stratified ambient waters located west of the Okaloosa Island Fishing Pier (red line in Figure 4). Warmer ambient water was entrained inside the bore through vertical mixing, which was suggested by a more gradual decrease in surface temperature (blue in Figure 12a). As the bore head propagated into very weakly stratified ambient waters, markedly smaller, westward ( $< -0.10 \text{ m s}^{-1}$ ) surface velocities than previous transects were identified at 17.2 UTC (Figure 12c). Values of  $\varepsilon$  decreased with depth in the near-surface region, indicated by shallow region values that ranged  $7.6 \times 10^{-6} \text{ m}^2 \text{ s}^{-3}$  to  $2.5 \times 10^{-5} \text{ m}^2 \text{ s}^{-3}$  and deeper values that ranged from  $2.9 \times 10^{-6} \text{ m}^2 \text{ s}^{-3}$  to  $6.2 \times 10^{-6} \text{ m}^2 \text{ s}^{-3}$  (grey boxes in Figure 12a and table in Figure 12b).

The ambient environment ahead of the bore was very weakly stratified, demonstrated by two (yellow and magenta in Figure 12e) nearly uniform density profiles that contained top-to-bottom values ranging from 1024.9 to 1025 kg m<sup>-3</sup>. Two density profiles collected in front of the internal bore displayed top-to-bottom density values ranging from 1024 to 1025 kg m<sup>-3</sup> (green profile in Figure 12e). One final CTD cast was collected behind the internal bore during this transect, which varied from 1022.7 to 1025 kg m<sup>-3</sup> from near the surface to the bottom. Low Richardson numbers were observed throughout the water column in most profiles ahead of the bore, which indicated mixed ambient water column conditions (Figure 12h).

Two vertical  $\varepsilon$  profiles (yellow and magenta in Figure 12i) were collected in the ambient, mixed waters ahead of the frontal zone. The profiles featured elevated  $\varepsilon$  values ( $8 \times 10^{-7} \text{ m}^2 \text{ s}^{-3}$ ) near 3 m depths and were influenced by vertical shears associated with converging surface flow. A VMP profile collected in the trailing edge of the bore (17.26 UTC) displayed the largest  $\varepsilon$  ( $5 \times 10^{-7} \text{ m}^2 \text{ s}^{-3}$ ) at 1 m, which linearly decreased beneath (cyan in Figure 12i). Three profiles (red, green, and blue in Figure 12i), collected behind the bore, showed active mixing which extended beyond the vertical extent of the bore rather than being confined to the near-surface region. This was identified by moderate values ( $0 \text{ } 10^{-7} - 10^{-8} \text{ m}^2 \text{ s}^{-3}$ ) throughout most of the upper 4 m of the water column.

### 3.3. River Plume Structure

The river plume observations (blue line in Figure 4) were collected after the frontal structure observations. The first indication of the river plume was observed at 17.64 UTC and featured a large near-surface temperature reduction ranging from 16.7°C to 14.3°C. A secondary reduction was observed at 18.1 UTC, which likely marked the beginning of a secondary front (Figure 13a). Initially from 17.67 UTC to 18.2 UTC, the river plume velocity was dominated in the east-west direction and featured westward velocities ( $\sim 0.20 \text{ m s}^{-1}$ ) in the upper 2.5 m (Figure 13b). Behind the bounding front of the plume (to the east), an internal bore was

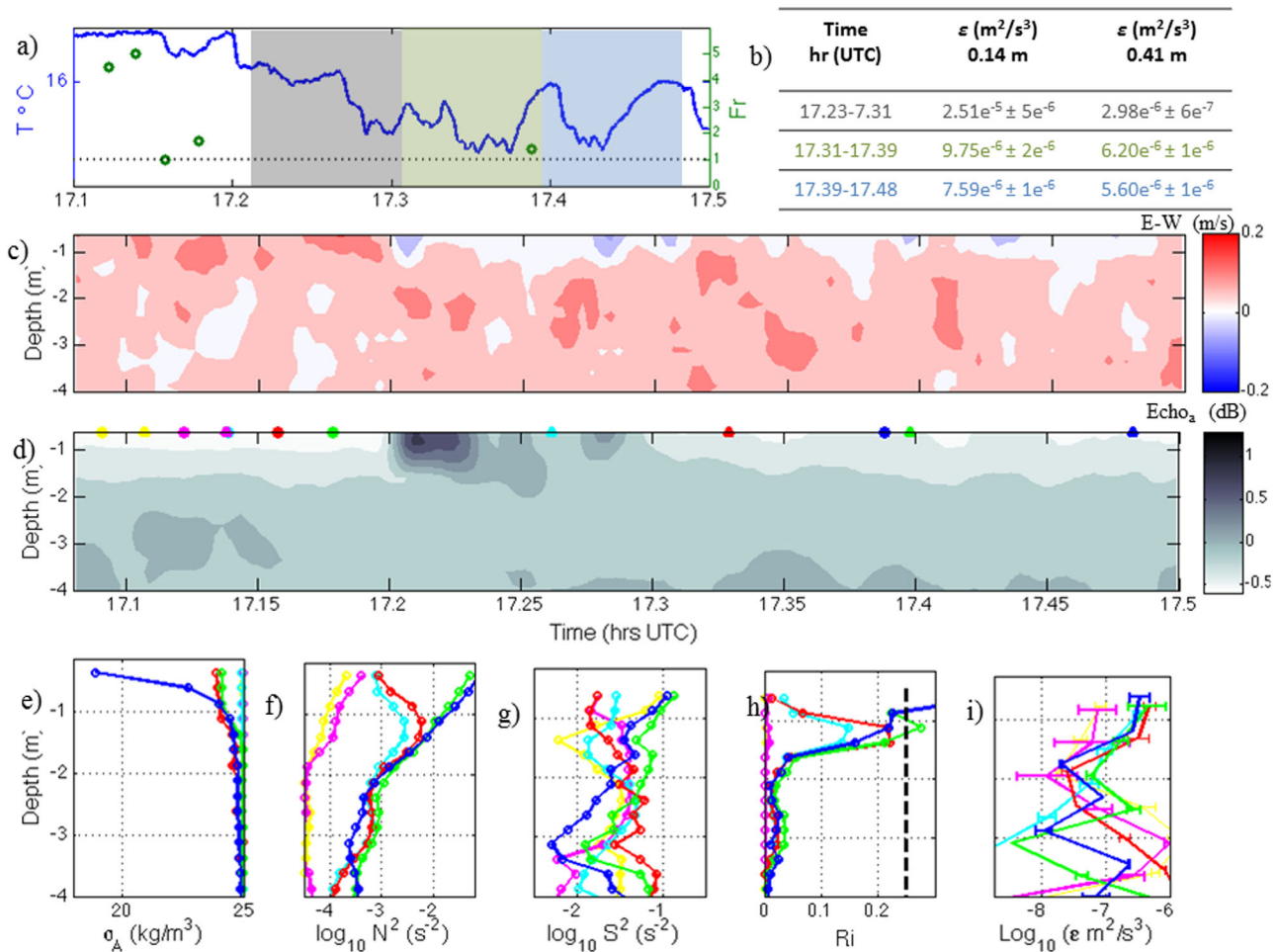


**Figure 12.** Frontal Transect FT3: (a) near-surface ( $\sim 0.10$  m) temperature (blue) and Froude number (green). Grey boxes mark periods corresponding to ADV  $\epsilon$  estimates; (b) table with  $\epsilon$  via ADV at 0.14 and 0.41 m depths, values correspond to time frame denoted by grey, green, and blue boxes,  $\pm$  represents 95% confidence limits; (c) east (red) and west (blue) velocity contours. The depth range has been truncated for plotting purposes and the actual depth is  $\sim 10$ ; (d) echo intensity anomaly, triangles denote VMP casts and circles mark CTD casts; (e) density anomaly,  $\rho - 1000$ ; (f) buoyancy frequency presented on a log base 10 scale; (g) squared vertical shear  $S^2$ , (h) Richardson number, black line is  $Ri = 0.25$ , values  $>0.25$  stable conditions and  $<0.25$  denotes conditions for mixing, and (i) TKE dissipation rates.

trailing the leading edge, determined by elevated echo intensity anomaly values  $\sim 0.5$  dB (Figure 13d). This finding was consistent with the presence of secondary wave-like disturbances behind main front [Pritchard and Huntley, 2002; Kilcher and Nash, 2010]. Closer to the inlet (after 18.2 UTC), the velocities inside the plume rotated to the southeastward direction. The ambient current beneath the river plume featured a region of accelerated eastward flow ( $\sim 0.15 \text{ m s}^{-1}$ ) that was  $\sim 835$  m in length from 17.86 UTC to 18.02 UTC before the secondary front (black-dashed line in Figure 13b). During this time, a single VMP cast was conducted (blue triangle in Figure 9d), where the vertical structure of  $\epsilon$  inside the plume revealed large values ( $6.3 \times 10^{-6} \text{ m}^2 \text{ s}^{-3}$ ) near the base of the plume (Figure 13e). This elevated  $\epsilon$  region developed from friction generated at the interface of opposing east-west flow. Large values ( $6.2 \times 10^{-6} \text{ m}^2 \text{ s}^{-3}$ ) were also observed near the bottom, which linearly decreased to ( $8.3 \times 10^{-9} \text{ m}^2 \text{ s}^{-3}$ ) at 4.5 m and suggested that the river plume does not “feel” the bottom at this depth.

### 3.4. Comparison to Gravity Current Theory

White and Helfrich [2008] developed a theory that explores gravity current speeds that result in internal wave generation under varying continuous stratification. The observed generation mechanism was consistent with “topographic” resonance, i.e., when the speed of the gravity current and speed of the first mode internal wave of the gravity current medium are similar.

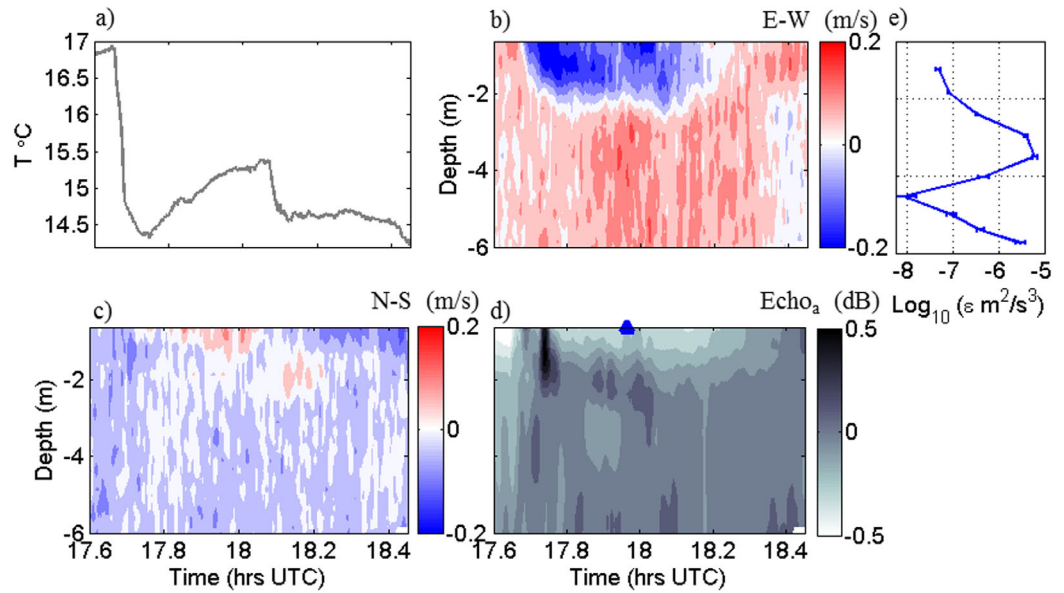


**Figure 13.** River Plume Transect RPT: (a) near-surface (~0.10 m) temperature, (b) east (red) and west (blue) velocity contours, (c) north (red) and south (blue) velocity contours, (d) echo intensity anomaly, (e) TKE dissipation rate presented on log base 10 scale. The y axes in Figures 13b through 13e are on the same scale.

Our observations indicated the bore head was detached in terms of velocity and density from the main body of the river plume (see conceptual diagram in Figure 14a), as opposed to being phased locked with the plume (Figure 14b). To determine if this scenario was plausible given the gravity current and ambient water properties, we created a wave-gravity current diagram (Figure 14c) following *White and Helfrich's* [2008]. A gravity current was implemented,  $U_{gc} = U \sqrt{S_p}$ , where,  $S_p = (\rho_2 - \rho_1) / (\rho_2 - \rho_c)$  is the stratification parameter,  $U = U^* / \sqrt{g'H}$  is the normalized speed of the gravity current,  $U^*$  is the translational speed of the gravity current,  $g = (\rho_1 - \rho_2) / \rho_2$  is the reduced gravity,  $H$  is the water depth,  $\rho_1$  is the upper density,  $\rho_2$  is the lower density, and  $\rho_c$  is the gravity current density, which was obtained from model output.

The bounding limit for internal wave detachment is determined by the Froude number  $U/c_1 = 1$ , while a lower limit denotes the *intrinsic* Froude number,  $Fr_i = U/c_0 = 1$ , where  $U$  denotes the normalized translational speed of the gravity current,  $c_0$  is the normalized first mode internal wave speed of the ambient waters, and  $c_1$  is the normalized first mode internal wave speed in the gravity current medium. Internal wave speed values are nondimensionalized by:

$$c_0 = \frac{c_0^*}{\sqrt{g'H}} \tag{12}$$

and

$$c_1 = \frac{c_1^*}{\sqrt{g'H}} \tag{13}$$

where  $c_0^*$  and  $c_1^*$  are dimensional values, and  $\sqrt{g'H}$  is a function of the ambient water.

This analysis was conducted assuming three ambient water column stratification scenarios, (outlined in the table in Figure 14c). The three cases investigated how increasing stratification would influence the potential for an internal bore to detach from the plume. Values of  $c_0$  were calculated using the Taylor Goldstein equation solver mentioned earlier, using density profiles calculated from an expression in *White and Helfrich* [2008]:

$$\overline{\rho(z)} = \rho_1 \left( 1 + \Delta\rho \left( 1 - \frac{\tanh(\lambda z)}{\tanh(\lambda)} \right) \right) \tag{14}$$

where  $\Delta\rho = (\rho_2 - \rho_1) / \rho_1$  and  $\lambda$  is a measure of nonuniformity of the stratification. We assumed  $\lambda$  to be small ( $\lambda = 0.5$ ) given the nearly linear ambient density profiles in FT2 (yellow in Figure 11e) and FT3 (yellow,

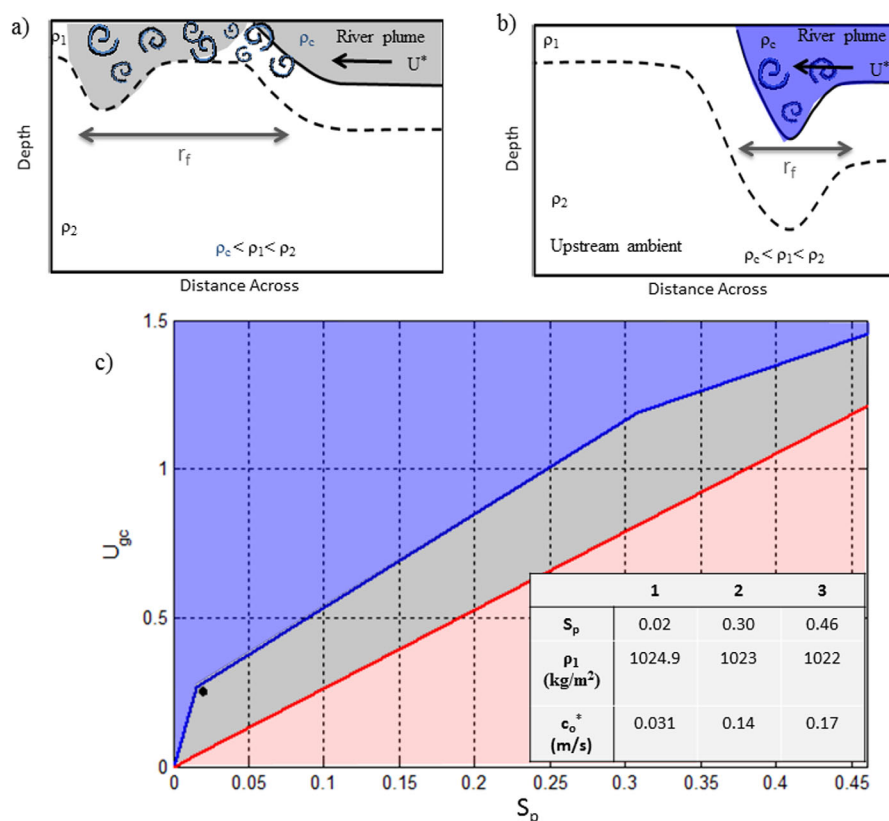


**Figure 14.** (a) Conceptual schematic depicting detached internal bore, grey area indicates freshwater, spirals are turbulent eddies,  $\rho_1$  is the upper layer density,  $\rho_2$  is the lower layer density,  $\rho_c$  is the density in the gravity current,  $U^*$  is the translational plume speed. This figure corresponds to grey area in Figure 15c, (b) depicts an internal bore that is phase locked with the river plume and corresponds to blue region in Figure 15c, (c) the wave-gravity current regime diagram.  $U_{gc}$  is a gravity current scaling, the blue bounding curve represents the upper threshold for wave generation, the red curve represents the subcritical threshold of the ambient environment, and the black dot represents the  $U_{gc}$  consistent with the observed river plume speed. Table displays regime diagram parameters:  $\rho_1$  is upper density reflecting three stratification scenarios: (1) very weak stratification, (2) weak stratification, (3) moderate stratification, and;  $c_0^*$  is the first mode internal wave speed of the ambient environment,  $S_p$  is the stratification parameter. The first mode internal wave speed of the gravity current medium was  $c_1^* = 0.21$  m/s, the lower density was  $1025$  kg/m<sup>3</sup>, the density in the gravity current was  $1018$  kg/m<sup>3</sup>, and the dimensional speed of the river plume was  $0.20$  m/s.

magenta in Figure 12e). The approximate global speed of the river plume,  $U^* = 0.2$  m s<sup>-1</sup>, was estimated using the alongshore (parallel to the coast) distance between the SAR image (11:28 UTC in Figure 4) and the GPS coordinates of the river plume front observed at 17.67 UTC in Figure 13. This estimate assumed a steady gravity current speed and does not account for local changes in speed.  $U_{gc}$  was calculated from  $U^*$  and plotted as a black dot in Figure 14c to determine if an internal bore could have detached.

This analysis showed that  $U^*$  resided in the grey wedge between  $U/c_1 = 1$  (blue curve in Figure 14c) and  $U/c_0 = 1$ , (red curve in Figure 15c). White and Helfrich [2008] found transcritical resonant forcing in this wedge region, where internal waves detached from the gravity current, consistent with the conceptual depiction in Figure 14a. White and Helfrich [2008] observed gravity currents speeds in the blue region (Figure 14c) featured a head wave phase locked to the river plume, consistent with the conceptual depiction in Figure 14b. Conversely, gravity currents speeds in the red region featured no head wave. This approach considers simplified conditions, in absence of many prevalent mechanisms in the coastal environment such as wind, tides, ambient currents, waves, etc., which could have modified the outcome.

### 3.5. Mixing Budget

A simplified budget was used to compare the relative influence of the wind, tides, and frontal mixing to the overall buoyancy input [Pritchard and Huntley; 2006]. Our observations enhance the work of Pritchard and Huntley [2006] by quantifying frontal zone mixing using direct estimates of  $\epsilon$  rather than a parameterization.

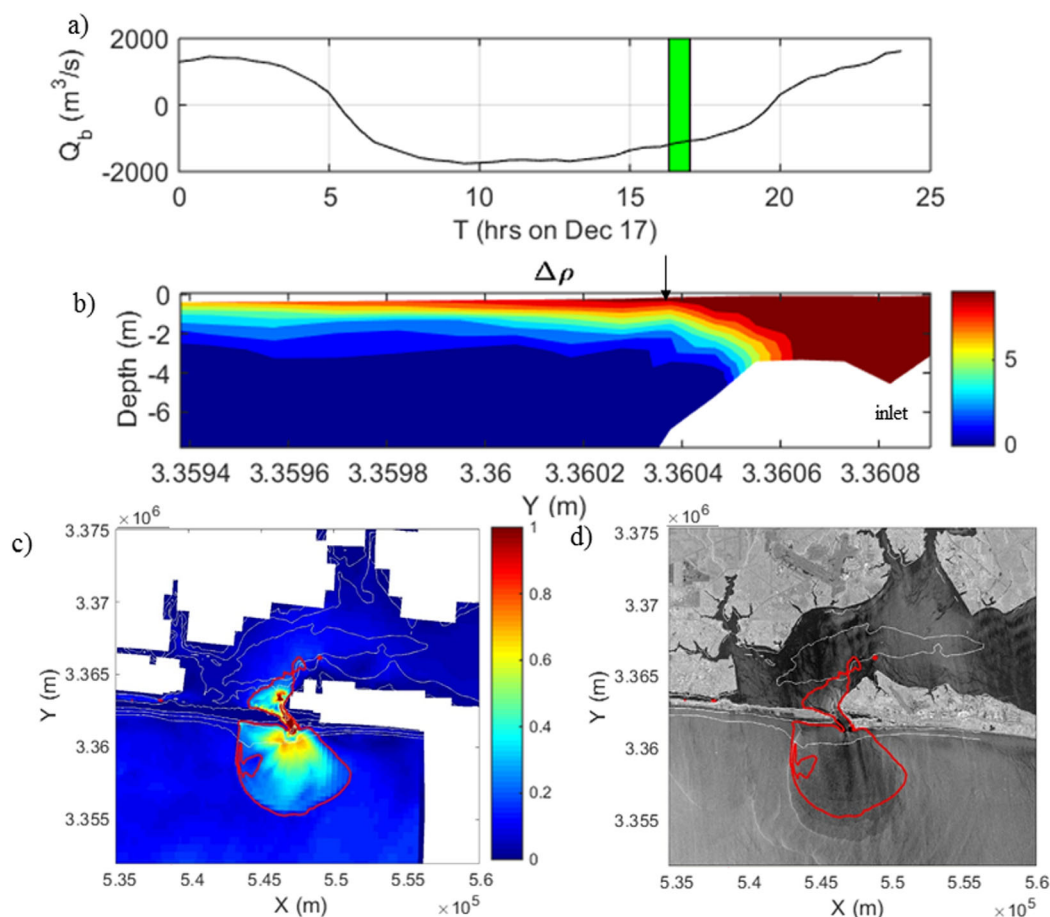


**Figure 15.** (a) The brackish water discharge from the model simulation, green box indicates in situ observations, (b) cross section of density anomaly (ambient minus plume density), black arrow indicates location where plume thickness and total water depth were taken for buoyancy power calculation, (c) model simulate corresponding to SAR overpass, filled contours are velocity magnitude, red contour indicates plume foot print (0.23 m/s), (d) SAR image with model plume foot print overlaid.

We were not able to provide an integrated energy budget as in *Pritchard and Huntley* [2006] because of the time-limited nature of our observations. This analysis does deliver instantaneous power estimates for the various mechanisms and leaves the opportunity for future observations that can resolve better tidal and spatial variability.

The amount of buoyancy input,  $P_b$ , during in situ observations (green in Figure 15a), was determined using the Delft 3-D model simulation, which provided the brackish water discharge ( $Q_b = 1150 \text{ m}^3 \text{ s}^{-1}$ ) for the inlet (Figure 15a). The density anomaly between ambient and plume water,  $\Delta\rho$  ( $9.4 \text{ kg m}^{-3}$ ), was also determined from model output just seaward of plume lift-off out of the inlet (black arrow in Figure 15b). Values of plume depth near inlet,  $d_{in}$  (3 m), versus total water depth,  $h$  (6 m), were also obtained at this location, which corresponded to the two-layer plume structure closest to the inlet discharge measurements. The instantaneous buoyancy input was calculated to be  $1.59 \times 10^5 \text{ W}$ . The mixing power due to tidal flow interacting with the bottom ( $P_t = 3.31 \times 10^4 \text{ W}$ ) and power due to wind stress at the surface ( $P_w = 2.77 \times 10^4 \text{ W}$ ), accounted for 21% and 17% of the buoyancy input, respectively. The values used to determine these parameterizes are detailed in Table 2. Uncertainties associated with these estimates were determined from the variation in wind speed, depth averaged ambient water current, and brackish river discharge during the observations (Table 3).

In order to quantify frontal mixing power,  $P_{FR}$ , a semi-elliptical ring was used to represent the frontal zone, which was estimated from the subtraction of two semi-ellipses. The larger semi-ellipse was estimated using the alongshore distance ( $a_{FR} = 8 \text{ km}$ ) of the final frontal measurement to the inlet (FT3 in Figure 4), which was combined with the aspect ratio,  $\gamma = 3.5 \text{ km}/7 \text{ km} = 0.5$  (Figure 6a), to calculate the across-shore

**Table 2.** List of All Parameters Used for Mixing Budget Analysis

Mechanism	Power (W)	% P <sub>B</sub>	Uncertainty Threshold (W)
P <sub>t</sub>	3.31 × 10 <sup>4</sup>	21	1.39 × 10 <sup>4</sup> to 4.18 × 10 <sup>4</sup>
P <sub>w</sub>	2.77 × 10 <sup>4</sup>	17	4.46 × 10 <sup>1</sup> to 5.58 × 10 <sup>3</sup>
P <sub>FR</sub>	9.39 × 10 <sup>4</sup>	59	6.87 × 10 <sup>4</sup> to 1.37 × 10 <sup>5</sup>
P <sub>B</sub>	1.59 × 10 <sup>5</sup>		1.49 × 10 <sup>5</sup> to 1.66 × 10 <sup>5</sup>

( $b_{FR} = 16$  km) distance. The frontal zone width,  $r_f = 260$  m, consistent with the conceptual depiction in Figure 6b, was estimated as the alongshore distance from the beginning of the frontal zone observations during Transect 2 (~16.6 UTC) to the end of the transect

(~17.05 UTC). The frontal zone depth,  $d_f = 2$  m, conceptually depicted in Figure 6b, was also taken from Transect 2. The second ellipse was smaller by  $r_f$  and the difference of the two yields a semi-elliptical ring that signifies the frontal zone surface area (grey ring in Figure 6a),  $A_{FR} = (\frac{\pi}{2} a_{FR} b_{FR}) - [\frac{\pi}{2} (a_{FR} - r_f)(b_{FR} - r_f)]$ . To obtain the mixing power in the frontal zone, the  $\epsilon$  values must be integrated with depth along the surface area of the frontal zone (grey shaded regions in Figures 6a and 6b). The  $\epsilon$  values used consisted of ADV estimates inside the internal bore in Transect 1, along with the shallowest two bins in the first VMP profile (green in Figure 10f), to construct a profile inside the bore. Next, the three ADV measurements of Transect 2 in the wake of the bore at 0.14 m and 0.41 m depths were combined with the closest three VMP profiles to construct  $\epsilon$  estimates for the upper 2 m of the water column in the bore wake (cyan, red, and black in Figure 11i). The  $\epsilon$  values were integrated with depth over  $A_{FR}$ . The power due to frontal mixing,  $P_{FR}$ , was estimated to be  $9.39 \times 10^4$  W, which was 59% of the total buoyancy input. Uncertainties associated with these estimates were evaluated using the variance between  $\epsilon$  estimates from the two orthogonal shear probes, which are displayed as error bars around all  $\epsilon$  profiles. A sensitivity analysis of the parameters used in the power calculations is detailed in the Appendix.

#### 4. Discussion

The frontal region of a weakly tidal, small-scale river plume was characterized using in situ measurements. The bore head was formed by the convergence zone of the river plume and opposing ambient current, which influenced very high  $\epsilon$  values ( $O 10^{-5} m^2 s^{-3}$ ). The near-surface values were four orders of magnitude larger than the ambient environment beneath and comparable to near-surface TKE dissipation rates generated by 13 m/s wind determined using the traditional “log layer” wind dissipation scaling [Csanady, 1984]. The elevated  $\epsilon$  surface values were compared with measurements from frontal regions of larger scale river plumes, including Orton and Jay’s [2005] Columbia River plume ( $6500 m^3 s^{-1}$  in Nowacki et al. [2012]) front values ( $\epsilon \sim O 10^{-4} m^2 s^{-3}$ ) and MacDonald et al.’s [2007] near-field Merrimack River plume ( $1260 m^3/s$ ) values ( $\epsilon \sim O 10^{-3} m^2 s^{-3}$ ). There is the potential for contamination in the ADV  $\epsilon$  estimates from surface wave orbital velocities and horizontal velocities associated with the bore. However, using the spectrum of vertical velocity fluctuations to estimate  $\epsilon$  (equation (2)) reduces the likelihood for horizontal velocities associated with waves to contaminate dissipation estimates [Huntley, 1988; Parra et al., 2014].

**Table 3.** Table Outlining Mixing Mechanisms<sup>a</sup>

Symbol	Name	Value	Units	Symbol	Name	Value	Units
$\delta$	Efficiency factor for tidal stirring	0.075		$A_f$	Area frontal zone	$8.52 \times 10^4$	$m^2$
$C_D$	Bottom drag coefficient	0.0025		$d_f$	Frontal zone depth	2	m
A	Surface area of plume	$4.02 \times 10^8$	$m^2$	$r_f$	Frontal zone width	260	m
$U_T$	Barotropic tidal current	$0.11 \pm 0.02$	$m s^{-1}$	$d_{in}$	Plume depth near inlet	3	m
$\gamma$	Aspect ratio	0.5		h	Total water depth at inlet	6	m
$\rho_2$	Ambient water density	1025	$kg m^{-3}$	$W_{10}$	Wind drag coefficient	0.00145	
$\Delta\rho$	Ambient versus plume density anomaly near inlet	9.4		$Q_b$	Instantaneous brackish discharge rate	1150	$m^3 s^{-1}$
$U_w$	Wind speed	$1.5 \pm 1$	$m s^{-1}$	$Q_R$	River discharge	150	$m^3 s^{-1}$
$\zeta$	Efficiency factor for wind stirring	0.023		$a_f$	Alongshore distance from the frontal zone to the inlet	8	km
$\rho_a$	Air density	1.225	$kg m^{-3}$	$b_f$	Across-shore distance from the frontal zone to the inlet	16	km

<sup>a</sup>Pt is tides, Pw is wind, PFR is frontal zone, PIF is interfacial and PB is buoyancy input. % are ratios of mixing mechanism to buoyancy input. The last column depicts uncertainty thresholds around estimates.

The head wave fundamentally represented an internal bore (propagating hydraulic jump) and featured a step like variation in near-surface temperature, followed by rapidly fluctuating values which suggested the bore was more dispersive than undular. Ultimately, these observations described an elevated dissipation frontal zone in the upper layer following the leading edge of the bore, which was fed by converging velocities at the bounding front. The bore head was detached from the river plume in terms of velocity and density structure. Not only was a discontinuity observed in westward near-surface velocities after the passage of the bore, but two density profiles collected in the wake during Frontal Transect 2 displayed increased upper layer densities. Later in time, the near-surface density reduced again, likely from the beginning of the freshwater lens of the trailing river plume and therefore supports bore detachment.

The detached internal bore observations were consistent with *Boyd et al.* [2010], who found that turbulent mixing in the wake of an internal bore propagating ahead of a tidal outflow from Loch Etive. The disturbed region featured values of  $\varepsilon$  that were two orders of magnitude larger than ambient conditions. The overall significance of bore head detachment is that it increases the energetic width of the frontal zone while the bore is in close proximity to the river plume. Our mixing budget results revealed that a longer frontal width increased frontal mixing input. Therefore, bore detachment could greatly enhance overall plume mixing. Over time, it is expected that the mixed energetic region behind the bore will have less influence on frontal mixing as the distance between the two increases.

*White and Helfrich's* [2008] gravity current theory determined that the head wave could have propagated away from the river plume given the observed ambient water conditions by the resonant interaction between the speed of the plume and the first mode internal wave speed of the medium inside the plume. We acknowledge that the potential for a bore to detach in a coastal environment may significantly vary from those predicted using the idealized hydraulic theory because of many external factors (currents, wind, tides, etc.). For a conceptual example, a pulse of onshore wind would restrict the offshore movement of the river plume, resulting in reduced plume speeds and potential bore detachment. However, the simplified theory would predict that internal bores could not detach if the river plume was purely driven by density gradients. Also, some of the assumptions used in the analysis may not be replicated in nature, i.e., conservation of energy, steady state, and hydrostatic pressure in the gravity current and ambient region. Moreover, there are a variety of other mechanisms that could have influenced the head wave to detach from the main body of the plume. The river plume could have propagated over a sharp bathymetric feature, which could locally cause the bore to detach for the plume. Secondary fronts have been shown to represent propagating wave-like disturbances ahead or behind the primary front [*Kilcher and Nash*, 2010; *Orton and Jay*, 2005]. It has been documented that they can form by shear instabilities trailing the bore head [*Garvine*, 1984], in addition to plume interaction with the coastal boundaries [*Garvine*, 1987].

The mixing budget revealed that the frontal zone could mix least 59% of the buoyancy input power, which is important in terms of coastal modeling. Given that coastal models do not accurately represent frontal processes due to grid resolution and other limitations, we compared the SAR image with the model derived plume footprint. Figures 15c and 15d depict the model output overlaid on the SAR image at the time the image was collected. Uncertainties between these locations was estimated at approximately 250 m. Surface velocity magnitudes are shown as filled contours, while the red contour outlines the head of the plume, where surface velocity magnitudes are approximately 0.23 m/s. The plume footprint observed in the SAR image was much larger than predicted by the model. This comparison displays plume processes 6 h before the in situ measurements, suggesting that this deviation may be even larger at the time of in situ observations. The spreading of a river plume is strongly correlated with frontal mixing. *Hetland et al.* [2010] found that when local mixing was reduced, plume spreading increased, which resulted in plume acceleration. Therefore, the model does not accurately predict frontal mixing, which resulted in a decelerated river plume and a smaller plume footprint. This observation supported the importance of frontal mixing in overall plume dynamics.

Beyond the uncertainties of the mixing budget estimates, which were a function of variability in the data, additional errors in these estimates could arise through assumptions in river plume surface area, as well as the frontal zone region. In our analysis, we assumed that the frontal zone extended across the entire perimeter of the plume, which assumed that across-shore dynamics were similar to alongshore dynamics and may not be the case. Additional errors could occur under the assumption that the river plume continued to spread symmetrically around the inlet as a semi-ellipse from 11:28 UTC to 17:30 UTC and maintained the

same aspect ratio. Therefore, if the plume were not spreading with the same aspect ratio, errors would emerge in the estimated ring area. We were not able to quantify the exact length of the frontal zone given our measurements, because our observations last until the main body of the river plume, which could yield an underestimation in the frontal zone mixing contributions. Even though there are a multitude of assumptions which could alter the mixing power from frontal processes, one important aspect emerges: frontal mixing is significant.

When the bore head detaches from a river plume, this indicates that the bore head travels faster than the decelerating river plume, until the bore eventually dissolves or transforms into internal waves. The formation process includes a buildup of energy at the head, where the amplitude increases, until it is large enough to propagate away from the plume. When the bore propagates away from the plume and becomes unstable, exhibiting dispersive behavior rather than undular, instabilities develop in the wake of the bore. This continues until the bore evolves into internal waves or disperses entirely. We propose that during this dispersive process, the length of the frontal zone will increase as the bore head propagates away from the plume (as in Figure 14 a). However, this only will occur for a period of time, until the bore head dissipates or evolves into nonlinear internal waves. The length of this period is, at present, unknown in context of river plumes. Given that the frontal mixing length,  $r_f$ , is used to determine frontal mixing power input, our results showed that the increasing disturbed region between the bore head and the plume increases the frontal mixing power of a river plume.

An improved understanding of these processes could be achieved by having multiple vessels simultaneously sampling the east, west, and offshore locations of the plume. However, this would require triple the resources available at the time of the SCOPE field campaign. Additionally, it would be valuable to have collocated  $\rho$  and  $\varepsilon$ , so that vertical eddy viscosity values could be quantified to provide a deeper understanding of mixing in the frontal regions, yet this was not possible due to sensor flooding on the VMP. It is critical to collect measurements that capture the evolution of the plume to properly evaluate the longevity of bore head detachment and its influence on plume mixing. Field observations could be paired with a nonlinear nonhydrostatic numerical model with capabilities to simulate bore head detachment, such as in *Stashchuk and Vlasenko* [2009]. These combined observations would determine the duration bore head detachment increases frontal mixing and overall plume mixing, which is important for developing a parameterization that can be implemented into coastal numerical models.

## 5. Conclusions

We have provided evidence that the frontal zone of a small-scale, weakly tidal river plume was important in coastal mixing. The frontal region featured a turbulent bore head, with elevated dissipation values ( $O 10^{-5} \text{ m}^2 \text{ s}^{-3}$ ) that were four orders of magnitude larger than the ambient values beneath. To the authors' knowledge, these  $\varepsilon$  measurements are the first reported in the frontal zone of a river plume in the northern Gulf of Mexico. The trailing energetic wake featured a disturbed surface region that contained elevated  $\varepsilon$  values, which formed an elevated dissipation frontal zone. Evidence supported that the bore head was detached from the main body of the plume. Typically, frontal zones are narrow ( $\sim 50\text{--}150$  m). As a bore head detaches, it propagates faster than the decelerating plume. A dispersive detached bore generates instabilities in the trailing wake, as observed, and should persist until the bore dissipates or evolves into nonlinear internal waves. The power generated by frontal processes is a function of the length of the frontal zone, therefore increasing frontal zones yield greater contributions to frontal mixing. Although the period for which this process occurs and significantly influences frontal mixing remains unknown.

The significance of bore head detachment is twofold: (1) bore head detachment likely expands the frontal zone for a period of time, which enhances the frontal influence in overall plume mixing and (2) the detached bore head could potentially transform into internal waves under optimal ambient water conditions. We found that while assuming uniform dynamics around the peripheral of the plume, the frontal zone was estimated to mix 59% of the buoyancy input, which highlighted the significance of this region and was consistent with *Pritchard and Huntley's* [2006] findings.

There are other estuarine outlets in the Gulf of Mexico that may contain energetic frontal zone such as the Choctawhatchee plume. Frontal zone processes could vertically mix surface-trapped in the case of another GOM oil spill, making it paramount that it is incorporated into oil spill forecasting. We have shown that

**Table A1.** Sensitivity Analysis Comparing Upper and Lower Thresholds of Parameters Used in Mixing Budget<sup>a</sup>

Parameter	Lower Bound	% of P <sub>b</sub>	Upper Bound	% of P <sub>b</sub>
P <sub>FR</sub>	8.81 × 10 <sup>4</sup> (W)	55	1.01 × 10 <sup>5</sup> (W)	64
P <sub>w</sub>	1.10 × 10 <sup>3</sup> (W)	0.6	3.08 × 10 <sup>4</sup> (W)	19
P <sub>t</sub>	4.82 × 10 <sup>3</sup> (W)	3	3.68 × 10 <sup>4</sup> (W)	23
P <sub>b</sub>	1.59 × 10 <sup>5</sup> (W)		1.59 × 10 <sup>5</sup> (W)	
δ	0.012		0.075	
ζ	0.001		0.023	
γ	0.55		0.45	

<sup>a</sup>δ is the efficiency factor for tidal stirring, ζ is the efficiency factor for wind stirring, and γ is the aspect ratio.

these narrow regions impact mixing, plume spreading, and internal wave generation, which emphasizes the need for representing these processes in regional circulation models.

### Appendix A: Sensitivity Analysis

A sensitivity analysis was conducted to evaluate various parameters used in quantifying power in the mixing

budget. Namely, the efficiency factor for tidal stirring, δ, the efficiency factor for wind stirring, ζ, and the estimated plume footprint aspect ratio, γ. Table A1 depicts the results of the sensitivity analysis. The expressions for δ and ζ are derived from the mixing and stratification model developed by Simpson and Hunter [1974]. The values represent the fraction of work contributing to mixing from either currents interacting with the bottom or wind blowing across the sea surface. Values of δ were found to vary from 0.012 to 0.02 in shelf seas [Bowman et al., 1983], while a value of 0.075 was determined in the Connecticut River plume [Valle-Levinson, 2010], which was used in for the mixing budget. Values of ζ were found to vary from 0.001 to 0.023 [Budéus, 1989] and a value of 0.023, to reflect a conservative estimate. The aspect ratio was varied to show a 90% confidence interval in plume surface area, yielding an aspect ratio ranging from 0.45 to 0.55. The results, presented in percentage of buoyancy input power, ranged from 3% to 23% for P<sub>t</sub>, 0.6% to 19% for P<sub>w</sub>, and 55% to 64% for P<sub>FR</sub>. This sensitivity analysis showed that modifying the efficiency factors and aspect ratio by justifiable and documented limits did not change the main message of the paper.

### Acknowledgments

This research was made possible by a grant from The Gulf of Mexico Research Initiative. Data are publicly available through the Gulf of Mexico Research Initiative Information & Data Cooperative (GRIIDC) at <https://data.gulfresearchinitiative.org>. The authors are thankful for the constructive comments provided by three anonymous reviewers. The authors would also like to thank Lauren Ross, Jackie Branyon, and Mike Rebozo for their help during fieldwork, in addition to Rob Hetland for his insightful comments and suggestions on the work.

### References

- Baumert, H. Z., J. Simpson, and J. Sundermann (2005), *Marine Turbulence: Theories, Observations and Models*, vol. 1, Cambridge Univ. Press, Cambridge, U. K.
- Blaylock, D. (1983), Choctawhatchee Bay—analysis and interpretation of baseline environmental data: Pensacola, Florida Sea Grant College, technical paper #29, 237 pp., 30 appendices.
- Bowman, M. J., A. C. Kibblewhite, S. M. Chiswell, and R. A. Murtagh (1983), Shelf fronts and tidal stirring in greater Cook Strait, New Zealand, *Oceanol. Acta*, 6(2), 119–129.
- Boyd, T., M. Inall, E. Dumont, and C. Griffiths (2010), AUV observations of mixing in the tidal outflow from a Scottish sea loch, in *Autonomous Underwater Vehicles (AUV)*, pp. 1–9, IEEE/OES, Monterey, Calif., 1–3 Sept., doi:10.1109/AUV.2010.5779670.
- Budéus, G. (1989), Frontal variability in the German Bight, *Sci. Mar.*, 53, 175–185.
- Canuto, V. M., Y. Cheng, A. M. Howard, and I. N. Esau (2008), Stably stratified flows: A model with No Ri(cr)\*, *J. Atmos. Sci.*, 65, 2437–2447, doi:10.1175/2007JAS2470.1.
- Chickadel, C. C., S. A. Talke, A. R. Horner-Devine, and A. T. Jessup (2011), Infrared-based measurements of velocity, turbulent kinetic energy, and dissipation at the water surface in a tidal river, *Geosci. Remote Sens. Lett.*, 8, 849–853.
- Crone, T. J., and M. Tolstoy (2010) Magnitude of the 2010 Gulf of Mexico oil leak. *Science*, 330, 634–643.
- Csanady, G. T. (1984) The free surface turbulent shear layer, *J. Phys. Oceanogr.*, 14, 402–411.
- Elgar, S., B. Raubenheimer, and R. T. Guza (2005), Quality control of acoustic Doppler velocimeter data in the surfzone, *Meas. Sci. Technol.*, 16, 1889–1893.
- Fedderson, F., J. H. Trowbridge, and A. J. Williams III (2007), Vertical structure of dissipation in the nearshore, *J. Phys. Oceanogr.*, 37, 1764–1777.
- Garvine, R.W. (1984), Radial spreading of buoyant, surface plumes in coastal waters, *J. Geophys. Res.*, 89, 1989–1996.
- Garvine, R. W. (1987), Estuary plumes and fronts in shelf waters: A layer model, *J. Phys. Oceanogr.*, 17, 1877–1896.
- Giddings, S. N., D. A. Fong, and S. G. Monismith (2011), Role of straining and advection in the intratidal evolution of stratification, vertical mixing, and longitudinal dispersion of a shallow, macrotidal, salt wedge estuary, 116(C03003), AGU, doi:10.1029/2010JC006482.
- Goodman, L., E. R. Levine, and R. G. Lueck (2006), On measuring the terms of the turbulent kinetic energy budget from an AUV, *J. Atmos. Oceanic Technol.*, 23, 977–990.
- Goring, D. G., and V. I. Nikora (2002), Despiking acoustic Doppler velocimeter data, *J. Hydraul. Eng.*, 1281, 117–126.
- Gruber, N., et al. (2011), Eddy-induced reduction of biological production in eastern boundary upwelling systems, *Nat. Geosci.*, 4, 787–792, doi:10.1038/ngeo1273.
- Hetland, R. D. (2010) The effects of mixing and spreading on density in near-field river plumes, *Dyn. Atmos. Oceans*, 49, 37–53.
- Horner-Devine, A. R., D. A. Jay, P. M. Orton, and E. Spahn (2009), A conceptual model of the strongly tidal Columbia River plume, *J. Mar. Syst.*, 78, 460–475, doi:10.1016/j.jmarsys.2008.11.025.
- Huntley, D. A. (1988), A modified inertial dissipation method for estimating sea bed stresses at low Reynolds numbers, with application to wave/current boundary layer measurements, *J. Phys. Oceanogr.*, 18, 339–346.
- Jay, D. A., J. Pan, P. M. Orton, and A. Horner-Devine (2009a), Asymmetry of Columbia river tidal plume fronts, *J. Mar. Syst.*, 78, 442–78,459, doi:10.1016/j.jmarsys.2008.11.015.
- Kilcher, L. F., and J. D. Nash (2010), Structure and dynamics of the Columbia River tidal plume front, *J. Geophys. Res.*, 115, C05S90, doi:10.1029/2009JC006066.

- Kourafalou, V. H., and Y. S. Androulidakis (2013), Influence of Mississippi River induced circulation on the Deepwater Horizon oil spill transport, *J. Geophys. Res. Oceans*, *118*, 3823–3842, doi:10.1002/jgrc.20272.
- Lien, R., and E. A. D'Asaro (2006), Measurement of turbulent kinetic energy dissipation rate with a Lagrangian float, *J. Atmos. Oceanic Technol.*, *23*, 964–976, doi:10.1175/JTECH1890.1.
- Livingston, R. J. (1986), Choctawhatchee River and Bay system, final report, vol. 1–4, Fla. State Univ. Cent. for Aquat. Res. and Resour. Manage., Tallahassee.
- Lueck, R. G., F. Wolk, and H. Yamazaki (2002), Ocean velocity microstructure measurements in the 20th century, *Jpn. J. Oceanogr.*, *58*, 153–174.
- Luketina, D. A., and J. Imberger (1987), Turbulence and entrainment in a buoyant surface plume, *J. Geophys. Res.*, *94*, 12,619–12,636.
- Lumley, J. L., and E. A. Terray (1983), Kinematics of turbulence convected by a random wave field, *J. Phys. Oceanogr.*, *13*, 2000–2007.
- Lyzenga, D. R., J. Johannessen, and G. Marmorino (2004), Ocean current and current boundaries, in *SAR Marine User's Manual*, edited by J. Apel and C. Jackson, U.S. Govt. Print. Off., Washington, D. C.
- MacDonald, D. G., L. Goodman, and R. D. Hetland (2007), Turbulent dissipation in a near-field river plume: A comparison of control volume and microstructure observations with a numerical model, *Geophys. Res. Lett.*, *112*, C07026, doi:10.1029/2006JC004075.
- Marmorino, G. O., and C. L. Trump (2000), Gravity current structure of the Chesapeake Bay outflow plume, *J. Geophys. Res.*, *105*, 28,847–28,861.
- Morris, J. G. J., L. M. Grattan, B. M. Mayer, and J. K. Blackburn (2013), Psychological responses and resilience of people and communities impacted by the deepwater horizon oil spill, *Trans. Am. Clin. Climatol. Assoc.*, *124*, 191–201.
- Nash, J. D., and J. N. Moum (2005), River plumes as a source of large-amplitude internal waves in the coastal ocean, *Nature*, *437*, 400–403, doi:10.1038/nature03936.
- Nowacki, D. J., A. R. Horner-Devine, J. D. Nash, and D. A. Jay (2012), Rapid sediment removal from the Columbia River plume near field, *Cont. Shelf Res.*, *35*, 16–28.
- O'Donnell, J., G. O. Marmorino, and C. L. Trump (1998) Convergence and downwelling at a River Plume front, *J. Phys. Oceanogr.*, *28*, 1481–1495.
- Ortiz-Suslow, D. G., B. K. Haus, N. J. Williams, N. J. M. Laxague, A. J. H. M. Reniers, and H. C. Graber (2015a), The spatial-temporal variability of air-sea momentum fluxes observed at a tidal inlet, *J. Geophys. Res. Oceans*, *120*, 660–676, doi:10.1002/2014JC010412.
- Ortiz-Suslow, D. G., K. Huguenard, N. J. Laxague, N. J. Williams, D. Bogucki, and B. K. Haus (2015b), Coastal dynamics observed from a Mobile Air-Sea Interaction Platform, paper presented at IEEE/OES Current, Waves and Turbulence Measurement Workshop, St. Petersburg, Fla.
- Orton, P. M., and D. A. Jay (2005) Observations at the tidal plume front of a high-volume river outflow, *Geophys. Res. Lett.*, *32*, L11605, doi:10.1029/2005GL022372.
- Pan, J., and D. A. Jay (2009), Effects of ambient velocity shear on nonlinear internal wave associated mixing at the Columbia River plume front, *J. Geophys. Res.*, *114*, C00B07, doi:10.1029/2008JC004988.
- Parra, S., I. Marino-Tapia, C. Enriquez, and A. Valle-Levinson (2014) Variations in turbulent kinetic energy discharge at a point source submarine groundwater discharge in a reef lagoon, *Ocean Dyn.*, *64*, 1601–1614.
- Pritchard, M., and D. A. Huntley (2002) Instability and mixing in a small scale estuarine plume front, *Estuarine Coastal Shelf Sci.*, *55*, 275–285.
- Pritchard, M., and D. A. Huntley (2006) A simplified energy and mixing budget for a small river plume discharge, *J. Geophys. Res.*, *111*, C03019, doi:10.1029/2005JC002984.
- Rippeth, T. P. and J. H. Simpson (1998), Diurnal signals in vertical motions on the Hebridean Shelf, *Limnol. Oceanogr.*, *43*, 1690–1696.
- Ross, J., I. Perez-Santos, A. Valle-Levinson, and W. Schneider (2014), Semidiurnal internal tides in a Patagonian fjord, *Prog. Oceanogr.*, *129*, 19–34.
- Ruth, B., and L. R. Handley (2006), Choctawhatchee Bay, in *Seagrass Status and Trends in the Northern Gulf of Mexico: 1940–2002*, edited by L. Handley, D. Altsman, and R. DeMay, pp. 143–153, *U.S. Geol. Surv. Sci. Invest. Rep.*, 2006-5287, 267 p.
- Sandstrom, H., J. A. Elliot, and N. A. Cochrane (1989) Observing group of solitary internal waves and turbulence with BATFISH and echosounder, *J. Phys. Oceanogr.*, *19*, 987–997.
- Seim, H. E., B. Kjerfve, and J. E. Sneed (1987), Tides of Mississippi sound and the adjacent continental shelf, *Estuarine Coastal Shelf Sci.*, *25*, 143–156.
- Simpson, J. H., and J. R. Hunter (1974), Fronts in the Irish Sea, *Nature*, *250*, 404–406.
- Smith, L. C., Jr., L. M. Smith, and P. A. Ashcroft (2010), Analysis of environmental and economic damages from British Petroleum's Deepwater Horizon oil spill, *Albany Law Rev.*, *74*(1), 563–585.
- Smyth, W. D., J. N. Moum, and J. D. Nash (2011), Narrowband oscillations in the upper Equatorial ocean. Part II: Properties of shear instabilities, *J. Phys. Oceanogr.*, *41*, 412–428, doi:10.1175/2010JPO4451.1.
- Stashchuk, N., and V. Vlasenko (2009), Generation of internal waves by a supercritical stratified plume, *J. Geophys. Res.*, *114*, C01004, doi:10.1029/2008JC004851.
- St. Laurent, L., M. H. Alford, and T. Paluszkiwicz (2012), An introduction to the special issue on internal waves, *Oceanography*, *25*(2), 15–19, doi:10.5670/oceanog.2012.37.
- Thatcher, M. L., and D. R. F. Harleman (1981), Long-term salinity calculation in Delaware Estuary, *J. Environ. Eng. Div. Am. Soc. Civ. Eng.*, *107*, 11–27.
- Tkalich, P., and E. S. Chan (2002), Vertical mixing of oil droplets by breaking waves, *Mar. Pollut. Bull.*, *44*, 1219–1229.
- Urick, R. J. (1983), *Principles of underwater sound*, 3rd edition, Peninsula Publishing, Los Altos.
- Valle-Levinson, A. (Eds) (2010), *Contemporary Issues in Estuarine Physics*, Cambridge Univ. Press, Cambridge, N. Y.
- Valle-Levinson, A., A. T. Castro, G. Gutierrez de Velasco, and R. G. Armas (2004), Diurnal vertical motions over a seamount of the southern Gulf of California, *J. Mar. Syst.*, *50*, 61–77.
- Valle-Levinson, A., K. Huguenard, L. Ross, J. Branyon, J. MacMahan, and A. Reniers (2015), Tidal and nontidal exchange at a subtropical inlet: Destin Inlet, Northwest Florida, *Estuarine Coastal Shelf Sci.*, *155*, 137–147.
- Wang, T., and T. Gao (2000), Internal tides, solitary waves and bores in shallow seas, *Chin. J. Oceanol. Limnol.*, *19*, 103–111.
- Wessel, P., and W. H. F. Smith (1996), A global self-consistent, hierarchical, high-resolution shoreline database, *J. Geophys. Res.*, *101*, 8741–8743.
- White, B. L., and K. R. Helfrich (2008), Gravity currents and internal waves in a stratified fluid, *J. Fluid Mech.*, *616*, 327–356.
- Xia, M., L. Xie, L. J. Piastrefesa, and M. M. Whitney (2011) The ideal response of a Gulf of Mexico estuary plume to wind forcing: Its connection with salt flux and a Lagrangian view, *J. Geophys. Res.*, *116*, C08035, doi:10.1029/2010JC00689.